Universiteit Utrecht

UMC Utrecht

Investigating blood-brain barrier leakage after photothrombotic stroke via DCE-MRI at 9.4T

Author: Maximilian Koprolin, BSc
Student Number: 4918614

January 2022

Major Internship (51 ECTS): Report
Master of Science: Neuroscience & Cognition
Track: Experimental- & Clinical Neuroscience
Faculty of Medicine
Graduate School of Life Sciences
Utrecht University

Daily Supervisor: Dr. Geralda van Tilborg, Biomedical MR Imaging and Spectroscopy Group, Image Sciences Institute, University Medical Center Utrecht, The Netherlands

First Examiner: Dr. Rick Dijkhuizen, Biomedical MR Imaging and Spectroscopy Group, Image Sciences Institute, University Medical Center Utrecht, The Netherlands

Second Examiner: Dr. Jaco J.M Zwanenburg, Department of Radiology, UMCU Brain Center, University Medical Center Utrecht, The Netherlands

Author Note

Maximilian Koprolin, Faculty of Medicine, Graduate School of Life Sciences, Utrecht University.

With special thanks to Dr. van Tilborg for providing me the opportunity to assist in her research and her unwavering mentorship. Further acknowledgements go to all members of the Biomedical MR Imaging & Spectroscopy Group that provided support throughout the entirety of the project.

Correspondence concerning the thesis should be addressed to Maximilian Koprolin

Contact: maximilian.koprolin@gmail.com

Table of Contents

Abstract

Post-stroke epilepsy (PSE) is a phenomenon in which patients experience two or more seizures one week or later upon suffering a stroke. While there is lack of scientific consensus regarding the etiology of PSE, there is evidence that blood-brain-barrier (BBB) disruption is a distinctive component of its origin. However, more insights are required to understand how BBB integrity mediates epileptogenesis. PSE is linked to poor functional recovery, and the sole treatment in use are antiepileptic drugs, which often lead to severe side effects. Thus, fully understanding the BBB integrity's mediating role in PSE is an important step towards developing alternative treatments. Additionally, novel prognostic tools that can discern stroke patients at risk of developing PSE are needed. Dynamic Contrast Enhanced MRI (DCE-MRI) allows the estimation of BBB permeability by modeling contrast agent (CA) leakage through the BBB in-vivo. Using this method, we aimed to characterize the spatiotemporal evolution of BBB integrity in relation to the development of PSE and identify MRI-based biomarkers that could predict the risk of acquiring PSE. To achieve this, we induced photothrombotic stroke in Sprague-Dawley rats, to mimic stroke in humans. Subsequently, the animals were scanned in a 9.4T MRI scanner, over various timepoints. Scans were conducted between 24 hours and 8 weeks post-procedure, using different concentrations of CA. The concentrations of CA present in the sagittal sinus and lesions were estimated via concentration mapping. Additionally, phantom scans were conducted, to validate in-vivo findings. Together, the data directly contributes to the optimization of DCE-MRI protocols at high field strengths, which can be adopted for a longitudinal study.

Keywords: Post-stroke epilepsy, stroke, DCE-MRI

Layman’s summary

Stroke is a global healthcare problem that is oftentimes accompanied with a plethora of complications. This illness arises when the brain is suffering from a lack of blood supply, either due to an artery being clogged or torn. One of the possible ailments a person can encounter after stroke is post-stroke epilepsy (PSE). This disorder is characterized by periodical seizures starting at least 7 days after stroke. In turn, these seizures further decrease the quality of life of the stroke patient. As of yet, we lack the ability to distinguish PSE risk groups amongst stroke survivors. Furthermore, we need to discover novel methods of treating the disorder. To do so, we first must comprehend how stroke leads to these reoccurring seizures. Evidence has been found that the blood-brain-barrier (BBB), which keeps harmful substances from reaching the brain, being disrupted by stroke may be a core cause of the disorder. In this study, we looked into the physiological changes of the stroke site over time using magnetic resonance imaging (MRI). We also employed dynamic-contrast enhanced MRI, in which a contrast agent is injected, to measure leakage across the BBB. Specifically, we attempted calculating how much of said contrast agent is present in a given location. The study was conducted by experimentally administering stroke in rats and then scanning them multiple times between 24 hours and 8 weeks after the procedure. Further, different concentrations of contrast agents were prepared and scanned to validate our estimations of contrast agent present in pre-defined areas of interest in the rat brain.

1. Background

1a. Blood-brain barrier

The blood-brain barrier (BBB) is a key player in the maintenance of brain homeostasis. Unique to the BBB are tight junctions between the bordering capillary endothelial cells in the brain, which restrict the influx of various molecules. This mechanism assists in maintaining both extravascular and vascular levels of ions and molecules at suitable concentrations. The molecular passage into the brain is arbitrated via a substance's ability to be lipid-soluble, as it needs to cross the endothelial cell membranes. Despite this, some non-lipid soluble molecules manage to enter brain tissue (e.g. glucose), as a result of specific transporters in the endothelial plasma membrane. Considering how delicate the brain's ionic environment is, the importance of the BBB cannot be emphasized enough, as it provides safety from potential toxins entering its parenchyma. As a result, BBB dysfunctions have been extensively studied. Numerous central nervous system pathologies have been linked to the passage of blood components in the extracellular space of the brain. One of these neurological dysfunctions being epilepsy (Abbott et al., 2010), in which it has been associated with the evolvement of the condition, i.e. epileptogenesis (Marchi et al., 2012).

1b. BBB role in Post Stroke-Epileptogenesis

One of the ways the BBB has been implicated with epileptogenesis is post-stroke epilepsy (PSE). This disorder is defined by the occurrence of at least two recurrent seizures not triggered by other causes such as toxicity or metabolism-linked seizures, at least 7 days after the stroke. The majority of PSE incidences are a result of arterial ischaemic stroke, as this type of stroke makes up 70-85% of cerebrovascular disease in adults (Feigin et. al, 2009). Nonetheless, it is in fact more likely that haemorrhagic stroke survivors develop PSE, as 10-20% of these strokes are epileptogenic, compared to 2-14% of the ischaemic strokes (Zhao et. al, 2018). A number of risk factors have been described in literature regarding the pathogenesis of PSE. The most prominent amongst these are younger age (<65 years) (Tanaka et al., 2015), cortical involvement (Silverman et al., 2002), a high National Institutes of Health Stroke Scale (NIHSS) score (Conrad et al., 2013), a high SeLect score (Galovic et al., 2018) and hypertension (Öhman, 1990, Wang et al., 2013). The presence of various genetic factors has also been linked to increased PSE likelihood, such as Rs671 (Mitochondrial aldehyde dehydrogenase 2) (Yang et al., 2014) and CD40-1 C/T (CD40 molecule, TNF receptor superfamily member 5) (Zhang et al., 2014).

While it is widely accepted that BBB disruption is a distinctive component of post-stroke etiology, how its integrity may mediate epileptogenesis is still under investigation. Additionally, other phenomena have been proposed as critical factors in epileptogenesis, such as heightened release of neurotransmitters, ion channel dysfunction and changes in gene expression. However, according to Tanaka & Ihara (2017), out of the phenomena that have been proposed to explain epileptogenesis after stroke, the BBB disruption hypothesis has been most verified (see figure 1 for visualization of the BBB disruption hypothesis). Essentially, it is purported that the BBB is impaired in a manner that it cannot complete its primary task of shielding the brain's ionic milieu from abnormal variations. Specifically, proteins and proteases circulating in the blood, such as albumin and thrombin, are allowed to enter the brain parenchyma, due to the decreased BBB impermeableness. Via growth factor TGF-β signaling

activation in astrocytes, albumin triggers a reduction of potassium and glutamate uptake leading to an aberrant restructuring of neural circuitry and excitatory synaptogenesis (David et al., 2009). The resulting hyperexcitability therefore promotes seizures. Further, the extravasated thrombin causes a surge in electrical activity and may induce seizures (Lee et al., 1997). We must also take into account that the interaction between BBB disruption and epileptogenesis is bidirectional, as the seizures may aggravate BBB dysfunction. For instance, Fieschie et al. (1980) found BBB breakdown during seizures in rats. Kim et al. (2012), also state that seizures may lead to brain inflammation, namely when astrocyte and microglial activation leads to the release of proinflammatory cytokines – which are associated with a distinct reduction in seizure threshold. This bidirectionality leads to a vicious circle promoting the evolution of PSE. Hence, the perfect storm is born for epileptogenesis.

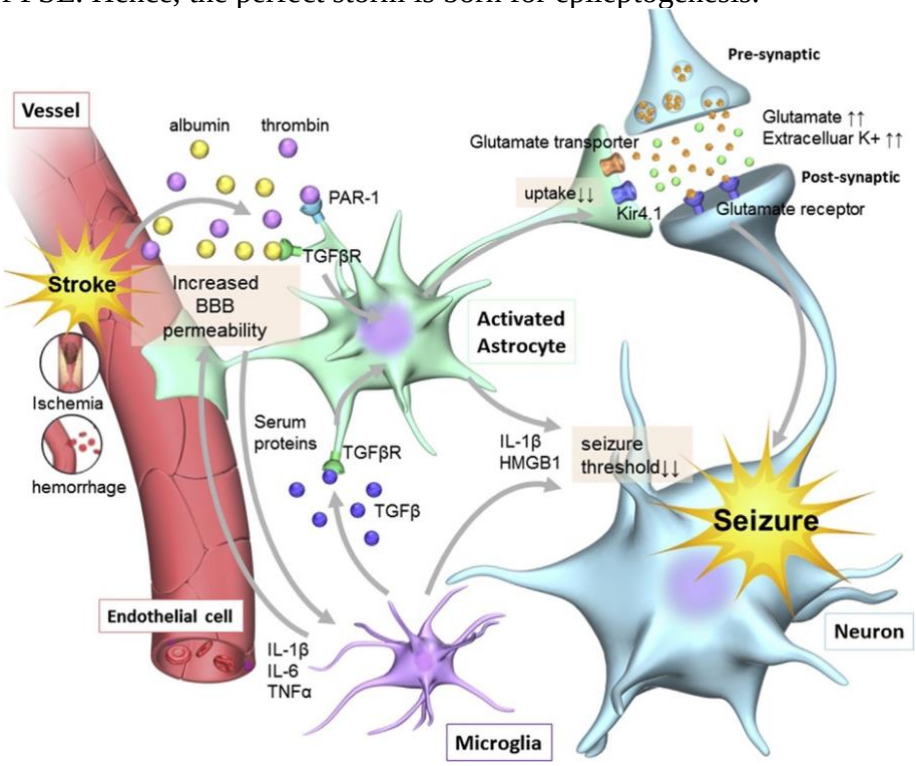

Figure 1. Illustration of post-stroke BBB disruption drawn from Tanaka & Ihara (2017)

1c. Photothrombotic stroke model

Despite the scientific progress in reference to our understanding of stroke comorbidities such as PSE, there is still much left to be discovered. The current obstacles to be overcome relate to the variability between articles regarding the incidence rate of stroke-related seizures, as these fluctuate between 2-20% in clinical strokes (Wang et al., 2017). As summarized by Altman, Shavit-Stein and Maggio (2019), in humans the reason for these discrepancies is based on the various stroke etiologies, differing definitions of PSE and diverging research protocols. However, with respect to pre-clinical studies in animals there is more experimental control, thus we can limit the influence of the abovementioned limitations. That being said, it still remains unclear whether there is a perfect animal model for PSE available as of yet. Further doubt is cast as to how translatable the findings are to clinical studies and potential drug development. *Table 1* details the techniques currently used in pre-clinical research to model stroke pathophysiology and induce PSE.

While the middle cerebral artery occlusion (MCAO) model is frequently used in stroke research, the photothrombotic stroke model has been the most successful in developing epilepsy in rats within and beyond two months post stroke. In this model, researchers

photochemically induce cortical thrombosis and brain infarction by means of injecting photosensitive dye followed by focal illumination through the intact skull (Kelly et al., 2001). This allows the researchers to impair blood flow in the superficial vessels exposed to light and to restrict injuries to their regions of interest, and investigate various predictive factors of epileptogenesis. The locus and severity of the lesion can be determined by the target of the applied laser and its light intensity/duration respectively.

Though BBB damage is a core pathophysiological feature of stroke, it has not been studied in detail beyond the acute stage of photothrombotic stroke (Hoff et al., 2005). Recent clinical accounts on the spatiotemporal characteristics of BBB opening post-stroke in humans have shown that it is highly intricate and can persist outside the acute stage of the ischemic injury (Nadareishvili et al., 2019). In fact, in animal models evidence has been found of augmented BBB permeability in regions that are untouched by the inceptive injury as a result of inflammatory reactions (Cao et al., 2020). Weber et al. (2020) have shown that within the photothrombotic model in mice, the majority of damage and vascular permeability is found at the lesion site and decreases proportionally with distance from the epicenter of the stroke and over time. Specifically, they discovered that at the infarct core, the leakage decreased marginally from day 1 (8.03 ± 3.83 mm2, $p > 0.05$), to day 7 (6.40 ± 2.20 mm2, $p > 0.05$) and day 21 (5.65 ± 2.80 mm2, $p > 0.05$). Further, leakage was not limited to this lesion core, but could also be found in perilesional areas, which they defined by vascular density ranging from 300 to 600μm from the stroke core. In these regions, a gradual decrease was detected from day 1 (5.79 ± 0.99 mm2) to day 7 (3.06 ± 1.13 mm2, $p = 0.007$), and day 21 (2.18 ± 2.01 mm2, $p = 0.001$). Respectively, they detected leakage on the contralesional cortex (2.39 ± 1.30 mm2) on day 1. However, this leakage dwindled to insignificant dimensions by day 7. Considering BBB integrity is linked to functioning adherens and tight junction protein complexes as well as pericytes (Berndt et al., 2019; Armulik et al., 2010), Weber et al. (2020) also investigated these components as possible contributors to vascular leakage. Indeed, they discovered an 80% decrease of pericyte fraction around blood vessels and a significant reduction of the surface ratio of blood vessels coated with tight and adherens junction complexes in the peri-infarct areas. Therefore, it was concluded that the BBB structure deteriorates even past the acute phase. Additionally, other researchers have also found evidence of leakage in areas distant to the lesion preceding seizures. For instance, Lippmann et al. (2017) detected abnormal signal hyperintensities on T2-weighted MRI images in the hippocampus in both hemispheres, within 24h post PT stroke. Likewise, after 7 days, BBB breakdown was confirmed via Evans blue extravasation in the hippocampus and perilesional tissue. Similarly, Lapilover et al. (2012), detected extravasation of Evans blue in the subcortical hippocampus, though mitochondrial metabolic function remained unaffected in the hippocampus at 12h after PT stroke.

Another interesting observation made in the PT stroke model, is the occurrence of mossy fiber sprouting. In humans, when researchers analyzed resected tissue to investigate hippocampal involvement in epilepsy, it was discovered that cells in the hippocampus of temporal lobe epileptic patients not only sustain seizure-related damaged, but that the plasticity of cells deviated from the norm. Both altered dendritic and spine morphology were observed, as well as considerable axonal sprouting of the mossy fiber system (Babb et al., 1991; Sutula et al., 1989). In fact, the sprouting of granule cell axons in human and certain experimental settings is a commonly observed feature in acquired epilepsies (Mathern et al., 1998). Indeed, when Karhunen et al. (2007) investigated epileptogenesis after PT stroke, they found such mossy fiber sprouting in the dentate gyrus of epileptic rats on both ipsi- and contralesional sides. Thus, when taking into account the BBB disruption, the possibility of mossy fiber sprouting and higher PSE occurrence rates of the PT model compared to other models, it is evident that the PT stroke model is a logical approach to take in investigating the BBB's role in post stroke epileptogenesis.

Animal Model	*Characteristics*	*Further information*	*Epileptogenic outcomes*	*References*
Middle cerebral artery occlusion (MCAo)	-Complex to administer -Medium mortality rate -High infarct volume	-Standard technique of vascular occlusion used in models of focal ischemic infarction -Produces large cortical/subcortical infarct ipsilateral to the occlusion.	-PSE occurrence rate: 0-25% -No mossy fiber sprouting -Limited success in demonstrating the development of PSE but the occurrence of early seizures more probable	(Reddy et al., 2017)
Common carotid artery occlusion (CCAo)	-Complex to administer -Medium mortality rate -High infarct volume	- Results in relatively large cortical infarcts of reproducible magnitude and area, without causing direct injury to the hippocampus. -Considered more invasive than MCAo techniques	-PSE occurrence rate: 0-14% -No mossy fiber sprouting -Better success in demonstrating PSE than MCAo techniques but inconsistent	(Engel, 2001; Kelly et al., 2006; Kelly et al., 2018)
Photothrombotic model	-Simple to administer -Low mortality rate -Low to high infarct volume	-Technically undemanding, minimally invasive method which can induce cortical brain infarction of reproducible size and location. -The model reproduces variety of features observed in human stroke but translatability to humans requires further investigation before AED development can begin.	-PSE occurrence rate: 35-50% -Mild mossy fiber sprouting -Seizures occur multiple weeks post stroke ipsilaterally to site of damage. Thus, more appropriate for PSE and not early seizures	(Engel, 2001; Kelly et al., 2001; Kharlamov et al., 2003; Watson et al., 1985)
ET-1 Vasoconstriction	-Simple to administer -Low mortality rate -Medium to high infarct volume	-Little to no breakdown of the BBB -Model cannot be confounded vasogenic edema in lesion formation -Effective in investigating mechanisms of ischemia-induced cytotoxic edema as well as the clinical studies of treatments preserving axonal integrity	- PSE occurrence rate: 0-8% -Mild mossy fiber sprouting -Minimal exogenous effects due to unaffected BBB -Generally, a weak trigger for epileptogenesis in adult rats. However, since higher doses of ET-1 may create greater infarction a high-dose regimen may increase PSE occurrence rates	(Hughes et al., 2003; Hallenbeck & Dutka, 1990, Karhunen et al., 2006)

Table 1. Pre-clinical research models for stroke pathophysiology and their PSE outcomes

1d. MRI-based assessment of BBB permeability

In order to understand why only a given percentage of stroke victims develop PSE, magnetic resonance imaging (MRI) can be a powerful tool in investigating BBB integrity deterioration as a function of PSE development. Specifically, the application of MRI may allow us to determine a number of predictive markers for PSE that could drive a great leap forward in personalized medicine and individualized treatment approaches. Such markers can be investigated via the monitoring of spatiotemporal shifts in BBB integrity, changes of functional neuronal connection and at the structural level. A benefit of this approach is that the pre-clinical experimental imaging data can be juxtaposed with clinical findings and novel effective protocols can be implemented in parallel to current techniques.

Particularly, Dynamic Contrast Enhanced MRI (DCE-MRI) enables us to estimate BBB permeability by modeling contrast agent (CA) leakage through the BBB in-vivo and in a noninvasive manner (Varatharaj et al., 2019). Gadolinium (Gd)-based CAs are commonly used for this purpose as they would not pass an intact BBB, thus making leakage an indicator for a compromised BBB. Typically, either low or high molecular weight CA are injected intravenously during repeated T1-weighted imaging acquisition or T1-mapping. The contrast material then accumulates in the extravascular extracellular space of the impacted tissue. Within this area, the agent's paramagnetic properties allow for shorten intrinsic T1 and T2/T2* relaxation times, which in turn increases signal intensity in T1-weighted sequences. Taking advantage of the T1 enhancement, DCE-MRI can distinguish and assess regions where the BBB is disrupted and quantify the degree of BBB disruption.

In terms of BBB permeability and integrity quantification, pharmacokinetic models drawing from nuclear medicine are frequently used. Concretely, the general two-compartment exchange model plays a core role, as it forms the basis for the various tracer kinetic models in use. Within this framework, the contrast agent is partitioned between intra- and extravascular compartments, which constitute the overall tissue volume (voxel) (Brix et al., 2004). Ultimately, the objective is to determine the two dynamic quantities, by means of which one may compute BBB permeability/integrity data. To exemplify, when the BBB is not disrupted the Gd should remain in the intravascular space and its movement through the space is a function of blood flow. In comparison, when the BBB is in fact disrupted, the Gd will not remain confined to the intravascular space. Instead, as previously mentioned, it will cross over and accumulate in the extravascular extracellular space, meaning the tracer concentration will increase, see figure 2 for a visualization. The corresponding kinetic data can be analyzed to reveal the extent to which the BBB is damaged.

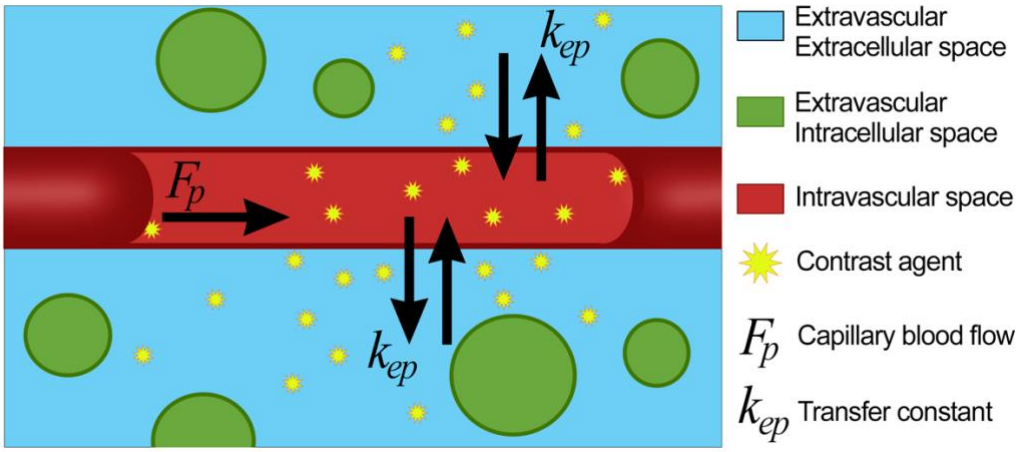

Figure 2. Illustration of a contrast agent crossing the BBB

Regarding the administration of the contrast agents, conventionally bolus injection protocols are used whereby a single, large dose of a substance is introduced venously, perfusing throughout the body during the scan and ultimately removed by the kidneys. As a result, there is a sharp spike in blood levels of Gd which subsequently declines rapidly. To avoid this rapid decline, step-down infusion protocols may be used, see figure 3 for an example (drawn from (Nagaraja et al., 2007). These also produce an initial sharp rise, but avoid the quick drop in contrast material levels by maintaining a constant contrast agent level throughout the imaging period (Nagaraja et al., 2007). This yields higher resolution and signal-to-noise ratios, as larger amounts of Gd are allowed to extravasate and remain present in plasma and tissue for longer amounts of time. As such, it may be superior in detecting acute BBB disruptions as compared to the regular bolus method, especially since it has previously been successfully employed in quantifying even mild BBB leakage via MRI during epileptogenesis (Vliet et al., 2013).

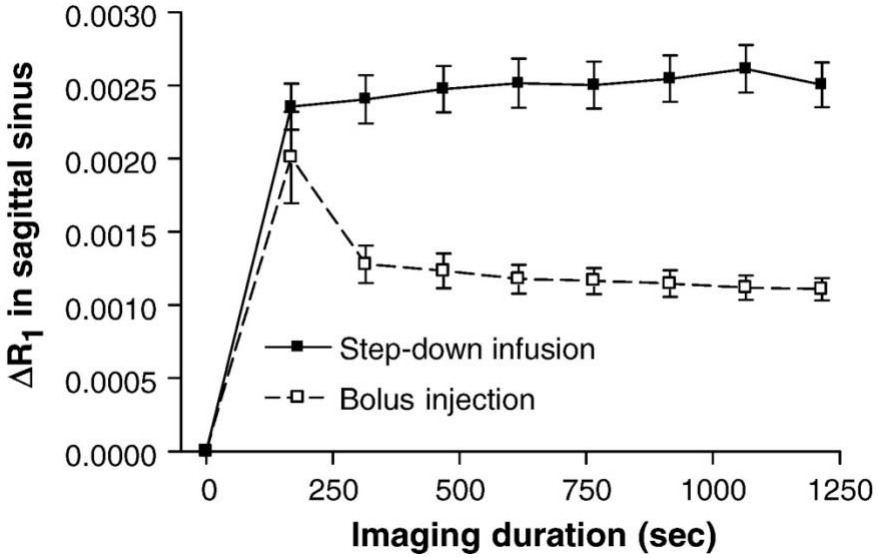

Figure 3. Example of changes in Gd levels over time in the sagittal sinus depending on infusion method (drawn from Nagarja et al., 2007)

1e. Aim of the study & research questions

Having outlined the current landscape of PSE research, it is evident that more insights are required regarding the manner in which BBB integrity mediates epileptogenesis. In fact, it

is necessary to fully understand this mediating role to identify novel targets treatments, either supplementing or replacing AEDs and establish substantiated prognostic tools that can discern PSE risk groups in stroke patient cohorts. This study serves as a pilot for a longitudinal study and aims to examine the feasibility of our approaches, which are intended to be used on a larger scale. Namely, we aim to optimize the PT stroke model for PSE, as well as the in-vivo delivery of Gd allowing the determination of BBB leakage sensitively, without introducing errors and to assess our DCE-MRI data quantitatively. Specifically, we seek to understand the manner in which the induced lesions evolve spatiotemporally, both in terms of morphology and BBB integrity. Here, the goal is to discern potential MRI-based biomarkers for PSE risk groups, but also to adjust the extent of the infarct. Further, we ask to what degree of precision we can acquire a quantitative index of contrast enhancement and infer Gd concentrations at ultra-high-field strengths, to determine which pharmacokinetic models may be relevant. As such, the photothrombotic stroke model was used to induce stroke in ten Sprague-Dawley rats, using varying stereotaxic coordinates. Subsequently, the animals were scanned using a DCE-MRI protocol over different time points between 24h-8 weeks post-procedure. Additionally, after sacrificing the animals, high-resolution post-mortem scans were conducted to gather more detailed anatomical data. Furthermore, two phantom experiments were performed to collect relaxivity data and measure signal enhancement at different Gd concentrations ranging from 0mm/L – 1.6mm/L. In the first phantom experiment, the contrast agent (CA) was diluted in manganese chloride (MnCl2), to match the intrinsic longitudinal and transverse relaxation times profile of tissue, whereas in the latter the CA was diluted in venous rat blood. The purpose of these phantoms was to allow us to describe the relationship between increasing CA concentrations and resulting signal intensity changes, to validate in-vivo findings. Lastly, CA concentration maps were generated to quantify the amount of of CA is present in the sagittal sinus and the lesion. Ultimately, this was a first step towards the application of relevant pharmacokinetic modelling necessary for the longitudinal study.

2. Methods & Materials

2.1. Samples

2.1a. In-vivo: experimental animals

Ten male Sprague–Dawley rats (Charles River, Germany) aged 10-11 weeks, weighing between 307–506g (Mean±standard deviation = 423±55.5) at the day of surgery, were used in this study. This was done in accordance with European Committee Council Directive of 24 November 1986 (86/609/EEC) and the experimental protocol was approved by the Local Ethics Committee. The animals were housed in a controlled environment with food and water available ad libitum.

2.1b. Phantom samples

In order to prepare the phantoms, a sample-holder (5x7cm) made of plexiglass was built. The sample-holder included 8 holes drilled on each short end, suitable to fit O.D L 2.5mm x 100mm NMR tubes (Wilmar NMR capillary tubes, Sigma-Aldrich Chemical Company, Milwaukee, WI, USA (Z558516-10EA)). Upon securing the tubes, the sample-holder was filled with 2% agar (2g in 100ml purified water) and left to cool, in order for the agar to solidify. See figure 4 for the finished product. Two sets of phantoms were prepared. For phantom

experiment 1, Gadobutrol/Gd-DO3A-butrol (Gadovist®, Bayer Ag) was diluted in a MnCl2 solution (10mg/L MnCl2 dissolved in demineralized water), replicating the T1 and T2 relaxation times of tissue as previously exemplified by Coolen et al. (2010). The tubes were filled with 8 different concentrations of CA, containing 0, 0.2, 0.3, 0.6, 0.8, 1.2 and 1.6mM of Gd. Regarding phantom experiment 2, they were filled with Gd diluted in venous rat blood, at the same 8 concentration levels. The blood was collected in a 4.5ml glass citrate tube with a 0.105M Na citrate additive (BD Vacutainer® glass citrate tube with light blue BD Hemogard™ closure, BD-Plymouth, UK), from one of the experimental animals before it was sacrificed. See appendix A for the serial dilution protocols.

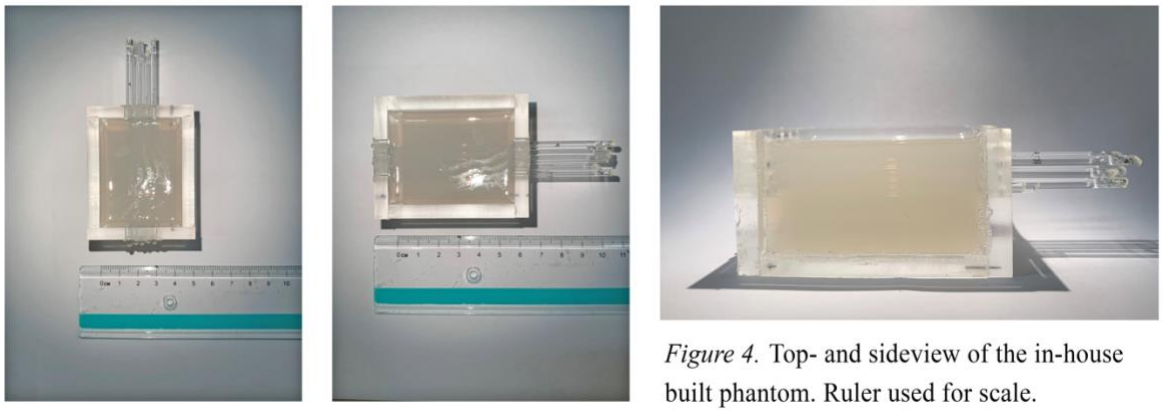

Figure 4. Top- and sideview of the in-house built phantom. Ruler used for scale.

2.2. Photothrombotic stroke

Rats were anaesthetized using either 5% isoflurane or a ketamine and dexmedetomidine injection, the latter being the preferred method, due to isoflurane's reported antiepileptic properties (Bar-Klein et al., 2016). The animals were then intubated for mechanical ventilation at 3% isoflurane in O_2/air (1:4) flow for rats not anesthetized via ketamine and dexmedetomidine. Once anesthetized, they were mounted to a stereotaxic frame, for precise placement of experimental tools at the defined coordinates. Lidocaine (0.1ml of 5% solution) and bupivacaine (0.1ml, 0.25% solution) were injected subcutaneously on the scalp prior to it being incised to expose the skull surface. During the operation, body temperature was kept at 37.0 ± 1.0°C using a self-regulating heating pad. The stereotaxic coordinates were adjusted over the course of the study, in order to yield lesions comparable to literature (e.g. Stoll et al., 2009; Kharmalov et al., 2003; Lapilover et al., 2012). An overview of both the coordinates and anesthesia methods per individual animal can be seen in *table 2*. Then, a catheter was inserted into the left Vena Saphena. Following the placement, 0.1µL/g body weight of the photosensitive dye Rose Bengal (25 mg/ml, Aldrich Chemical Company, Milwaukee, WI, USA) was infused at 0.225ml/min via this catheter.

Rat number	Stereotaxic coordinates	Anesthesia method and antidote dosage	In-vivo scan timepoints	Post-mortem scans (Yes/no)
1	1.5mm L; 0mm AP (marking center)	Ketamine (490.8µL) & dexmedetomidine (389.3) **Antidote**: none	24h	No
2	1.5mm L; 0mm AP (marking center)	Isoflurane	24h	No
3	2mm L; -3.6mm AP (marking center)	Isoflurane	7 days, 15 days, 4weeks	Yes
4	2mm L; -3.6mm AP (marking center)	Isoflurane	6 days, 13 days, 4 weeks	Yes
5	2.2mm L; -1.8mm AP (marking center)	Ketamine (309µL) & dexmedetomidine (245µL) **Antidote**: Atipamezole (1 injection at 1mg/kg)	Died after surgery	No
6	2.2mm L; -1.8mm AP (marking center)	Ketamine (298.5µL) & dexmedetomidine (237µL) **Antidote**: Atipamezole (7 injections at 0.1mg/kg and 1 injection at 0.2mg/kg)	24h, 3 weeks, 8weeks	Yes
7	2.2mm L; -1.8mm AP (marking center)	Ketamine (195µL) & dexmedetomidine (158µL) **Antidote**: Atipamezole (3 injections at 0.2mg/kg)	48h, 8days, 8 weeks	Yes
8	2.2mm L; -1.8mm AP (marking center)	Ketamine (198,5µL) & dexmedetomidine (160,7µL) **Antidote**: Atipamezole (3 injections at 0.2mg/kg)	48h, 8days, 14days, 8weeks	Yes
9	2.2mm L; -1.8mm AP (marking center)	Ketamine (246.5µL) & dexmedetomidine (199.6µL) **Antidote**: Atipamezole (3 injections at 0.2mg/kg)	24h	Yes
10	2.2mm L; -1.8mm AP (marking center)	Ketamine (253µL) & dexmedetomidine (204.8µL) **Antidote**: Atipamezole (5 injections at 0.2mg/kg and 1 injection at 0.4mg/kg)	24h	Yes

Table 2. Overview of procedures per rat

Once the required amount of rose bengal was infused, a cold light source (Schott KL 1500LCD, Germany), placed straight on the skull surface was switched on. The brain was illuminated through the intact skull for 20 mins in a darkened room, see figure 5 for a visual illustration. Afterwards, the catheter was removed and the wounds were sutured. The rats were allowed to awaken in a heated recovery cage. Once they regained mobility, they received buprenorphine (0.05mg/kg) as well as the antidote atipamezole of dexmedetomidine (given they were anesthetized using ketamine & dexmedetomidine) to reverse its sedative effect. Afterwards they returned to their cages.

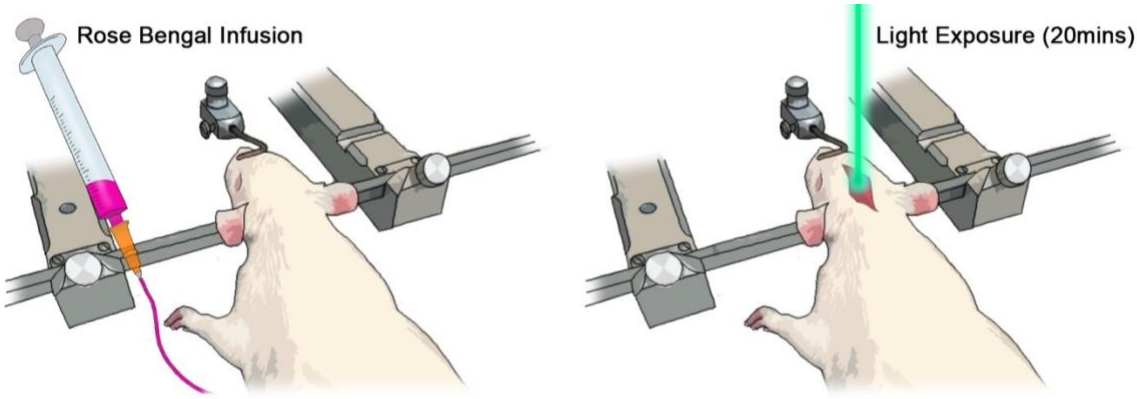

Figure 5. Schematic of PT procedure

2.2a. Inclusion criteria

As previously mentioned, and detailed in *table 2*, the stereotaxic coordinates were adapted in order for the lesions to match those shown in literature (Stoll et al., 2009; Kharmalov et al., 2003; Lapilover et al., 2012). Due to the variability in anesthesia method, stereotaxic coordinates and scanning timepoints, data from rat 1-4 will not be included in the analysis. Hence, the in-vivo data analyzed regarding anatomical changes is exclusively based on rat 6-10 (*n*=5). In this sub-sample, rat 6-8 were studied for 8 weeks after PT stroke was induced and rat 9 and 10 were only investigated for 1 week. Thus, the sample of experimental animals available for this aspect of the study is *n*=5 for week 1 and *n*=3 for week 8.

2.3. MRI protocols

2.3a. In-vivo scanning protocol

In vivo MRI measurements were conducted using a 9.4T preclinical MR system using a 400mT/m gradient coil (Varian/Agilent). The setup was equipped with a home-built 90mm diameter Helmholtz volume coil for signal excitation and an inductively coupled 25mm diameter surface coil for signal reception. Thereafter, they were anesthetized with 5% isoflurane and then endotracheally intubated for ventilation with 2% isoflurane in O_2/air (1:4). Further, a catheter (0.38mm ID, 1.09mm OD) was placed in the tail vein for latter CA administration. Then, a singular dose of 100µL of saline with 2.5 µL/ml of heparin were injected. Once the rat was placed in the scanner, respiration rate was monitored, CO_2 levels and blood oxygenation were tracked via a capnograph and a pulse oximeter respectively. Body temperature, was kept stable at 37.0 ± 1.0 °C. Anatomical images were acquired via a balanced steady-state free precession (BSSFP) sequence (TR=5ms, TE=2.502ms, flip angle=20°, isotropic spatial resolution of 250µm, FOV=40x32x24mm^2). Thereafter, pre-contrast data

necessary for DCE-MRI was acquired via the following scans: B1-map (TR=5ms, TE=4ms, flip angles=60° & 120°, interleaved FOV=4x3.2cm^2, matrix=80x32, 24 slices, 1mm slice thickness) to adjust for flip angle deviations, a Look-locker T1-map (TRimage=6ms, TE=3.25ms, TR=10ms, 34 images, matrix=128x64, FOV=32x32, 16 slices, interleaved) to acquire T1 times before CA infusion and a T1-weighted sequence (TR=10ms, TE=1.8340ms, flip angle=20°, matrix=80x128x96, FOV=40x32x24, glimPE=35%, 3 repetitions) to measure signal intensities before the administration of Gd.

2.3b. In-vivo contrast-enhanced imaging

Having acquired the anatomical images and pre-contrast images, Gd was then infused from a 5ml syringe (11.99 ID, BD Emerald) filled with 0.3, 0.6 or 0.8mM/Kg of Gd and saline via the catheter in the tail vein. The initial step-down infusion protocol was adopted from Nagaraja et al. (2007). However, it was adjusted to deliver 50% less total volume (1.75ml) over the 20 minutes of infusion due to the first two animals' negative physiological reactions to such high influx liquid volume entering their bodies. The final protocol (see *table 3*) was automated via the programmable interface of a Chemyx Fusion 100 infusion pump (Chemyx Inc, Stafford, United States).

Step	Volume (ml)	Rate (ml/min)
1	0,17	0,34
2	0,13	0,265
3	0,195	0,195
4	0,14	0,14
5	0,11	0,11
6	0,095	0,095
7	0,15	0,085
8	0,21	0,07
9	0,3	0,06
10	0,25	0,05

Table 3. Step-down infusion protocol

At the exact point that the infusion pump was activated, scanning was resumed. Specifically, the T1-weighted sequence (TR=10ms, TE=1.8340ms, flip angle=20°, matrix=80x128x96, FOV=40x32x24, glimPE=35%, 3 repetitions) was continued to be acquired, in order to measure the changes in signal intensity throughout the Gd infusion. Once the acquisition was completed, the rat was removed from the scanner and placed in a heated recovery cage until it regained function. A visual depiction of the MRI acquisition can be seen in appendix B. The infusion line was then flushed with saline and air to clean it, after which it was filled with the corresponding Gd dilution for the following animal.

Given it was the final timepoint for a rat to be scanned, the experiment was terminated by perfusion-fixation for subsequent post-mortem scanning. Specifically, the animal was heavily sedated using isoflurane after which the abdomen was incised to expose the heart via the diaphragm and a needle was placed into the aortic arch. Then, the perfusion pump was switched on to perfuse 150ml of saline with heparin (1ml/L) and the right atrium was cut to allow blood to leave the system. Once the saline with heparin was depleted, the input of the pump was switched to 250ml of 4% paraformaldehyde (PFA) (in phosphate buffer) which was then also perfused. Afterwards, the needle was taken out, the animal's head was decapitated

and both skin and eyes were removed. The rat's brain, including its skull, was placed in 50ml falcon tubes filled with 4% PFA for 7 days for post-fixation. After 7 days it was transferred to another 50ml falcon tube containing phosphate buffered saline (PBS) with 0.05% azide solution.

2.3c. Post-mortem protocols

Post-mortem high-resolution structural MRI scans were acquired ≥ 7 days after the brains were transferred to PBS/azide. Imaging was conducted via the same 9.4T preclinical MR system, with the gradient and coil being substituted by a 6 cm internal diameter gradient insert with gradients up to 1 T/m and a custom-made solenoid coil with an internal diameter of 2.6 cm respectively. The perfusion-fixed brains were placed in a custom-made holder and immersed in non-magnetic oil (Fomblin, Solvay Solexis). Thereafter, four 3D BSSFP images were acquired with an isotropic spatial resolution of 75µm (TR=15.4ms, TE=7.7ms, flip angle= 40°, 426x214x256 matrix, FOV 31.9x16.1x19.2 cm^3, 12 averages at pulse angle shift 0°, 90°, 180° and 270°). The four images were added as complex images to obtain a single BSSFP image without banding artifacts in the brain.

2.3d. Phantom protocols

Phantom measurements were conducted using the exact same scanner setup as the in-vivo scans. The aforementioned sample-holder, containing the eight samples was placed in the scanner. Thereafter, scanning commenced immediately. Firstly, B1-maps were acquired (TR= 8ms, TE=4ms, flip angles=60 & 120°, interleaved, FOV=4x3.2 cm^2, matrix=80x32, 24 slices, 1mm slice thickness) to correct for B1 inhomogeneity over the field of view, by measuring the actual flip angle. Following this, a multiple echo multi shot (Mems) T2-map (TR=6000ms, TE=7ms, NE=80, 1 average, 2 dummy scans) to measure T2, a multiple gradient echo multi slice (Mgems) T2*-map (TR= 2000ms, TE=3ms, TE2=3.5ms, 40 echoes, flip angle=90°, 1 average, 2 dummy scans) to measure T2* and a Look-locker T1-map (TR=3ms, TE=3.25ms, 2 averages, TRimage=6ms, flip angle=5°, 2 dummy scans, 400 inversion samples, 1 slice) to measure T1 were acquired to compute the corresponding relaxivity data. Lastly, a T1-weighted image (TR=10ms, TE=1.834, matrix=80x128x96, FOV=40x32x24, flip angle=20°) was acquired to observe signal intensities. The temperature of the samples was not controlled for.

2.4. Image processing & analysis

2.4a. In-vivo image analysis

The in-vivo BSSFP images were registered to a reference image, namely an in-house template, generated from a previous study. The registration process was automated using a script developed in MATLAB (version R2019b), utilizing numerous tools from the FSL software package (http://www.fmrib.ox.ac.uk/fsl/, Smith et al., 2004): Firstly, the nonparametric nonuniform intensity normalization (N3) algorithm was applied for bias field correction. Following this, the images were spatially deformed, in order to achieve a more spherical and approximate the dimensions of a human brain. This was done with the purpose of removing the skull from the image via the FSL brain extraction tool (BET) (Smith, 2002), leaving only the region occupied by brain tissue and surrounding tissue, which is optimized for human brains. Once the skull was removed, the image was resized to its original dimensions and a mask was created of the brain. Thereafter, FMRIB's Linear Image Registration Tool (FLIRT) (Jenkinson et al., 2002) was used to linearly register the input image to its reference image. Upon completing linear registration, segmentation was performed via FMRIB's Automated Segmentation Tool (FAST) (Zhang, Brady & Smith, 2001) which segmented the

image into its different tissue types. This allowed for the ventricles to be removed from the mask, to limit interference caused by the lesions or stroke-related ventricle deformations. Lastly, FMRIB's Non-Linear Image Registration Tool (FNIRT) (Andersson, Jenkinson & Smith, 2010) was run to compensate for anatomical differences, thus improving the quality of the registration and in turn allowing for inter-subject comparisons.

Furthermore, ROIs were drawn manually over the lesion sites of each individual anatomical in-vivo scan, to calculate the lesion volumes at different time points and compute an average. In order to characterize how the lesion developed over time, a lesion incidence heatmap was created for week 1 and 8. To achieve this, we firstly drew a ROI of the contralesional cortex used to normalize signal intensities across the registered images. Thereafter, the images were averaged and all lesion masks were combined via a MATLAB script, which merged each matrix value of the masks and expressed the percentage rats that had lesioned tissue in the given area.

Lastly, in order to generate CA concentration maps, further registrations were conducted. Namely, T1-map and B1-maps were registered to the anatomical BSSFP images, as these have better resolution and yield superior registrations compared to immediate registration to the T1-weighted images. In turn, the BSSFP was registered to the T1-weighted images and the resulting the transformation matrix was used to put T1-maps and B1-maps from BSSFP space into T1-weighted space. For visual representation of these steps, see appendix C. Additionally, a mask of the sagittal sinus and the lesion were drawn in T1-weighted space. The relevant images were then used as input for a MATLAB script, which was based on the methodology and equations shown by (Lee et al., 2018).

2.4b. Phantom image analysis

Similarly, to the in-vivo scans, the first analysis step was a N3 bias field correction, in the T1-weighted sequence. Thereafter, for all other sequences a ROI was manually drawn for all phantom scan images at the center of each tube. The resulting binary masks were then multiplied with their corresponding images via fslmaths creating masks that contain the values within each tube. The mean of non-zero voxels in these non-binary masks was then calculated using fslstats, thus giving us the average T1, T2, T2* values and T1w signal intensities from the T1-map, T2-map, T2*-map and T1-weighted scans respectively, for each one of the phantom samples. The resulting data was then used to derive relaxation rates ($R1 = \frac{1}{T1}$, $R2 = \frac{1}{T2}$, $R2^* = \frac{1}{T2^*}$) as well as signal enhancement. Additionally, the B1-maps were registered to the T1-weighted images, with the purpose of correcting for B1 inhomogeneity related flip angle deviations, which could lead to signal intensity errors and lower T1 weighting.

2.4c. Signal equations for simulated signal intensities

The signal from a spoiled-GRE sequence depends on three operator-specified parameters (TR, TE, and flip angle α) as well as intrinsic tissue parameters T1 and T2*. The T2* dependence is directly tied to the length of the TE; the longer the TE, the larger the T2*-weighting. As such, the steady-state signal equation for our T1w sequence is given by (1):

$$S = k\,\frac{\sin\alpha\,(1-\,e^{-\frac{TR}{T1}})}{(1-(\cos\alpha)\,e^{-\frac{TR}{T1}})}\,e^{-\frac{TE}{T2*}}$$

However, as exemplified by Busse (2005) in an ideal condition, where transverse relaxation is fully spoiled after each excitation and T2* effect is negligible (TE << T2*), is oftentimes assumed resulting in the following equation (2):

$$S = \frac{\sin \alpha \, (1 - \, e^{-\frac{TR}{T1}})}{(1 - (\cos \alpha) \, e^{-\frac{TR}{T1}})}$$

As such, through the data acquired from the T1-maps and T2*-maps of the phantoms, we can model signal enhancement using these signal equations, thereby highlighting the effect of T2* at low and high CA concentration levels. Additionally, via the B1-maps, a correction term can be calculated by substituting the ideal α in equation 1 with the observed α in the B1-maps, correcting for given flip angle deviations.

3. Results

3a. CA infusion & anesthesia optimization

In both rat 1 and 2, in which the original step-down infusion protocol by Nagarja et al. (2007) was implemented, it was discovered that the rats began to have negative physiological reactions (i.e. deviations in heart rate and respiration rate) halfway through the infusion protocol. Hence why we designed a new infusion protocol by halving the amount of liquid infused, which solved the issues of the initial method. Furthermore, rat 5 could not be included due to a fatal reaction to the antidote to the anesthesia (i.e. the buprenorphine & atipamezole) after the procedure. The dosage of the antidote was thereafter decreased and no more fatalities occurred.

3b. Primary in-vivo structural changes

Figure 6 shows the lesion incidence at 24-48 hours (referred to as week 1) and week 8 of with each slice being five slices apart from another, starting rostrally and moving caudally. Here, we can clearly observe a decrease in lesion volume. However, the inner core of the lesion at week 1 remains damaged after 8 weeks, whereas the peripheral areas show signs of recovery. Additionally, at 8 weeks post-procedure we can discern hyperintensity below the lesion site. Within week 1 after PT stroke was induced, the lesion volumes ranged from 82.125 – 31.468 mm^3 (Mean±standard deviation = 57.2mm^3 ± 19.3mm^3, n=5). At the 8-week timepoint, the lesion volume was between 20.9 – 9.9 mm^3 (Mean±standard deviation = 15mm^3 ± 5.5mm^3, n=3), thus resulting in a 63.46% decrease in lesion volume between week 1 and 8.

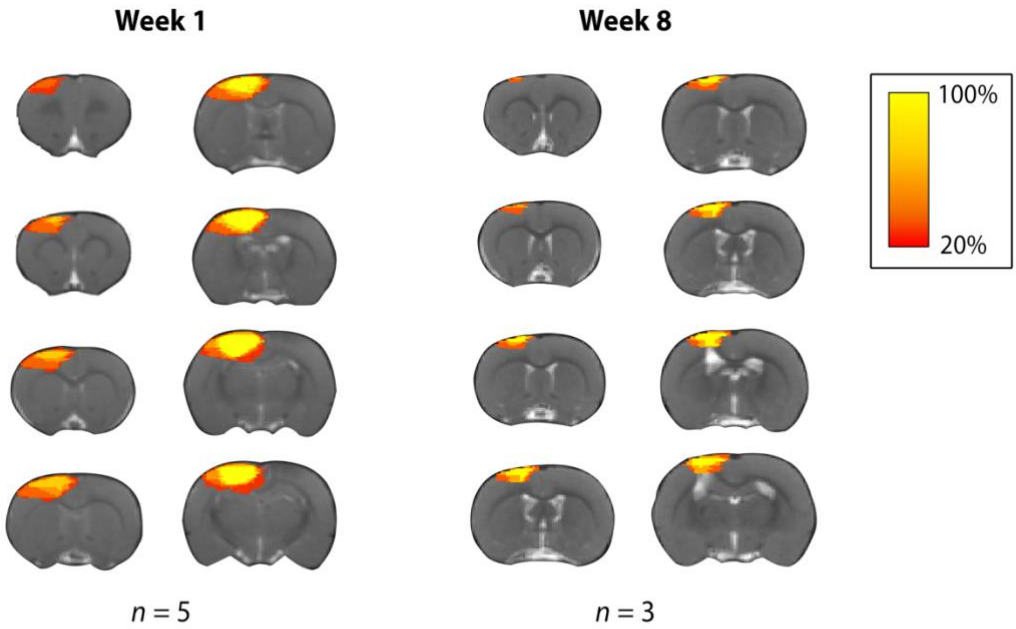

Figure 6. Lesion incidence on coronal slices at week 1 and week 8 in percent of rats affected in a given area.

Further, the lesioned area at the week 1 timepoint were defined against cortical ROIs. This was only done for this timepoint, as reorganization is to be expected in the ipsilateral hemisphere over the ensuing weeks. Below, figure 7 breaks down the lesioned areas percentagewise, defined against our ROIs. The lesioned tissue outside of our ROIs was visually inspected via the Paxinos-Watson anatomical rat atlas (Paxinos & Watson, 2005), and it was determined that these regions included the retrosplenial dysgranular cortex (RSD), secondary visual cortex, mediomedial area (V2MM), secondary visual cortex mediolateral area (V2ML), primary visual cortex (V1).

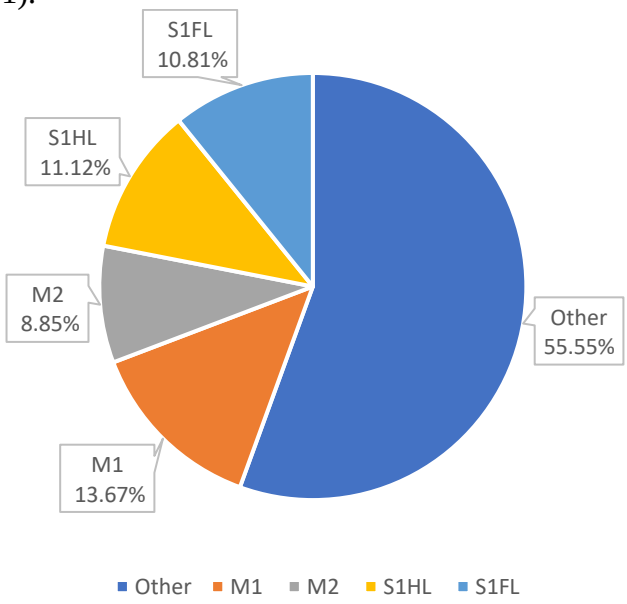

Figure 7. Percentage of ipsilateral cortical ROIs lesioned one-week post stroke. *M1* = primary motor cortex, *M2* = secondary motor cortex, *S1FL* = primary somatosensory cortex forelimb region, *S1HL* = primary somatosensory cortex hindlimb region, Other = lesioned areas not included in cortical ROI's used in this study

Additionally, when looking at individual in-vivo BSSFP scans at the 8-week timepoint, we were able to discern secondary thalamic injury, as highlighted in figure 8.

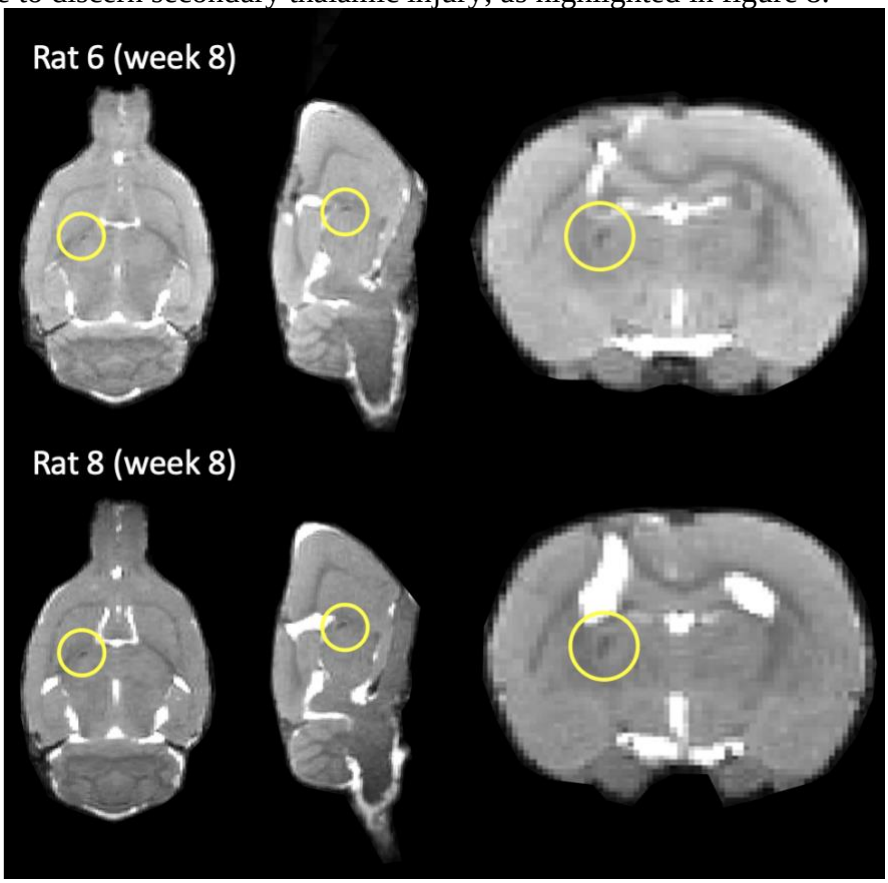

Figure 8. In-vivo BSSFP scans week 8, showcasing secondary thalamic injury

3c. High-resolution post-mortem scans

Similarly, the post-mortem scans clearly show secondary thalamic injury at both the 4- and 8-week timepoint as seen in figure 9. As such, we can assume that this form of secondary damage may become visible already at 4 weeks post-stroke. Upon visually inspecting this thalamic degeneration, and comparing it to the Paxinos-Watson anatomical rat atlas (Paxinos & Watson, 2005), we determined the affected sub-regions of the thalamus. Namely, at the 4-week timepoint, in rat 9 the damage reached the ventral posterolateral thalamic nucleus (VP), the ventrolateral thalamic nucleus (VL) and the laterodorsal thalamic nucleus, ventrolateral (LDVL), and at the 8-week timepoint in rat 6 the damage also reached the LDVL.

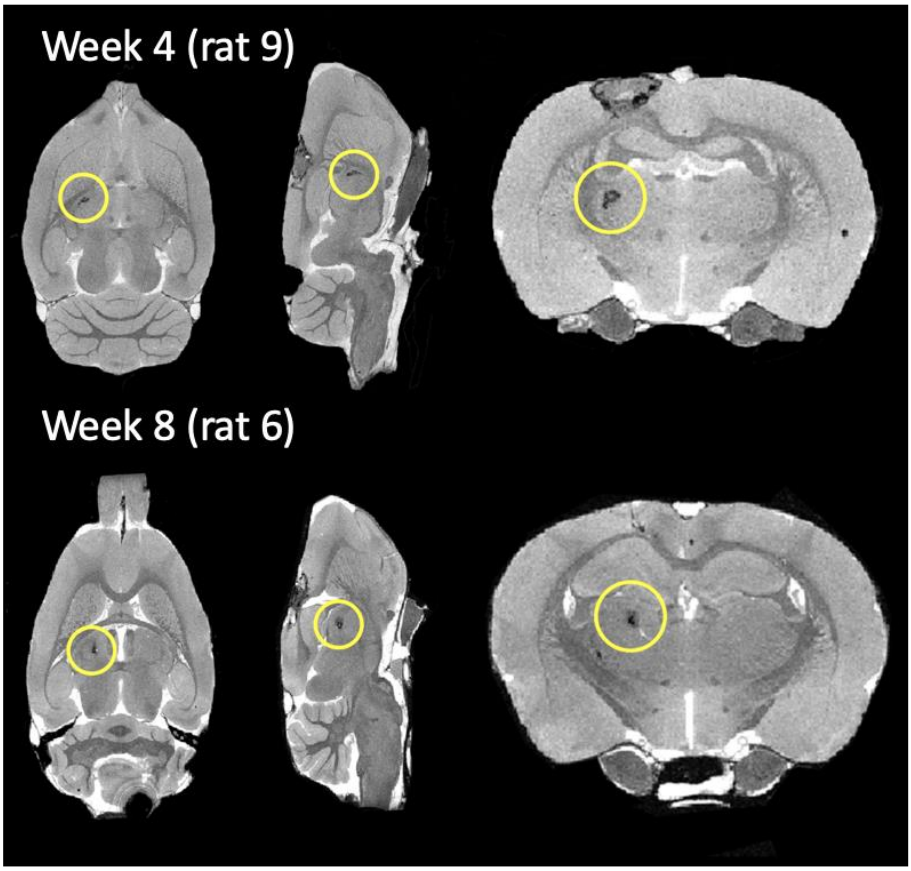

Figure 9. Post-mortem BSSFP scans (75µm isotropic resolution), week 4 & 8

3d. Phantom scans: relaxometry

Regarding the phantom data, we first calculated the relaxation times by averaging the values within the ROI masks of each tube in the T1-, T2- and T2* maps. The inverse of each longitudinal relaxation time ($\frac{1}{T1}$) within the phantom tubes was plotted and fitted linearly to obtain an r1 of $4.2 s^{-1} mM^{-1}$and $5.7 s^{-1} mM^{-1}$ respectively for the MnCl2- and blood phantom. The longitudinal relaxivity curve of Gd in MnCl2 can be seen below figure 10. The same process was repeated to calculate r2 ($\frac{1}{T2}$) and r2* ($\frac{1}{T2*}$) values. For the MnCl2 phantom an R2 of $6.2 s^{-1} mM^{-1}$ and a R2* of $5.1 s^{-1} mM^{-1}$ were determined. However, when attempting to compute the R2 and R2* for the blood phantom, no linearity could be identified and will not be shown below. As such, the blood phantom data had to be discarded. Likewise, increases in signal intensity measurements from our T1-weighted sequence in both phantoms were inconclusive, which will be further addressed in the discussion.

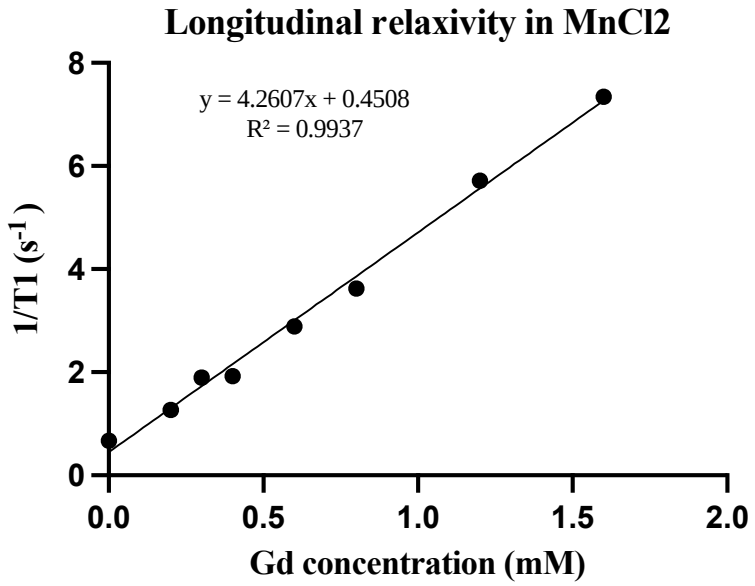

Figure 10. Longitudinal relaxation rates in the MnCl2 phantom experiment

3e. Simulated phantom SI

To circumvent the obstacles the phantom scans provided, we had to fully simulate the SIs for the T1-weighted sequence. Using the previously mentioned signal equations (1, 2) we modelled Gd-based signal enhancement taking into account, or neglecting T2* decay. Assuming that the values derived from the T1 and T2* maps for phantom experiments 1 were accurate, we only had to draw the T1 and T2* values in venous blood at 9.4T from literature. Using the literature-based T1 and T2*, we then simulated signal intensity using the r1 and r2* values we measured in phantom experiment 1 (i.e. MnCl2). According to Deistung et al. (2008) r2* of venous blood increases exponentially with B0 and its T2* is equal to 97ms, 21.2ms and 7.4ms at 1.5T, 3T and 7T respectively. Thus, due to the lack of availability of relaxation time and rate of venous blood at higher field strengths such as 9.4T in literature, we had to also model this value. Under the assumption that r2* of venous blood indeed increases exponentially with B0, we could thus infer that at 9.4T the T2* equals 2.33ms and the corresponding R2* is $429.44 s^{-1} mM^{-1}$. Further, we based the T1 relaxation time on the T1 in oxygenated blood at 9.4T (2429ms) as stated by Dobre, Ugurbil & Marjanska (2007), given that oxygenation level does not significantly affect blood T1 (Lin et al., 2012).

In panel A of figure 11, we can see our models, with the modelled SIs of our phantoms scattered over the signal enhancement curves. In line with Hagberg & Scheffler (2013), we can observe the three phases of (I) linear and nonlinear signal increase; (II) plateau; (III) T2 or T2*-related signal decay. As expected, the signal decay is only visible in the models that actually take T2* into account, as the diminishing signal is related to TE, tissue T2* (TE << T2*) and r2 relaxivity of the CA. Thus, when T2* is neglected in the equation, no such drop in signal will be observed. Due to the signal decay, concentration levels beyond maximal contrast enhancement, determined by the r1 and r2 of the CA, TR as well as the flip angle, are trivial for contrast-enhanced MRI. As such, when looking at clinically relevant concentration levels (i.e. panel B of figure 11), we can see that signal intensity increases uniformly in tissue whether we take T2* into account or not. Yet, in blood an immediate deviation can be distinguished as a result of T2*.

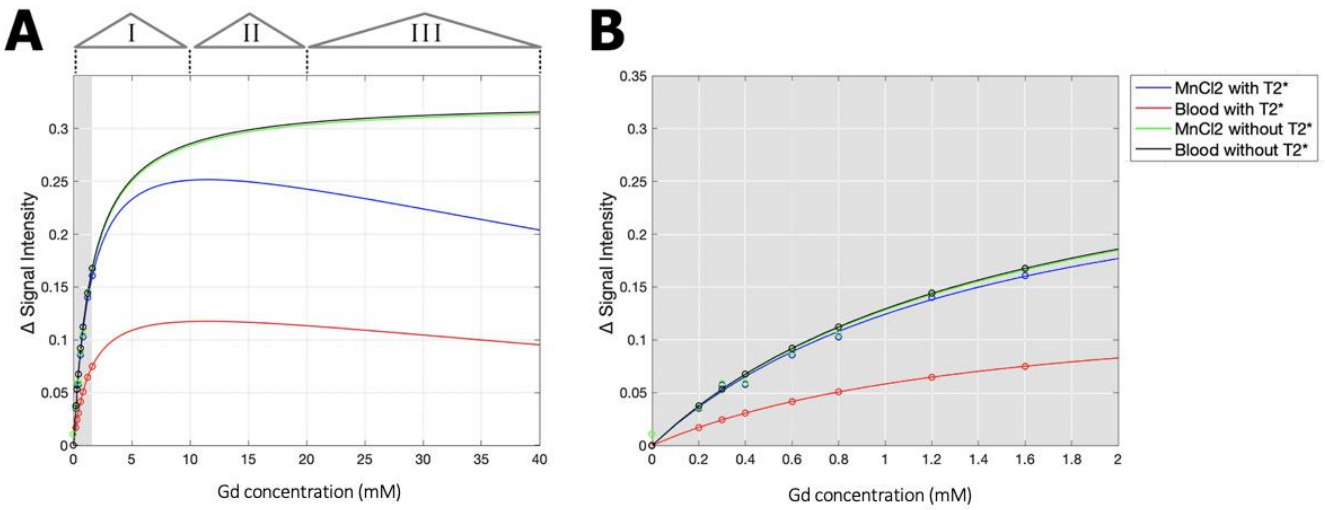

Figure 11. Modelled SI enhancement as a function of CA concentration with the SIs of both phantoms scattered.

3f. Estimating Gd concentration in sagittal sinus

Firstly, the SI changes throughout the infusion protocol were visualized in the form of a timeseries in both the sagittal sinus and the lesion sites, per concentration of Gd infused (see figure 12). Important to note here is that for the lesions, only week 1 data was utilized, in order to maintain a consistent sample without interference from cortical re-organization. As such, the neither the 0.6mM, nor two of the 0.3 and 0.9mM concentrations could be included, since this data was acquired past 1-week post-stroke. Within the sagittal sinus we could discern that peak SI was reached halfway through the acquisition. In contrast, within the lesion, SI increased at a slower rate and only peaked during latter timepoints of the acquisition. Further, the timeseries of the sagittal sinus allowed us to clearly distinguish the higher concentrations infused (0.6 & 0.8mM) from the 0.3mM concentration, as higher SI was achieved throughout the majority of the acquisition. When looking at the timeseries of the lesion, all SIs increased in a more uniform manner, with the exception of one of the 0.8mM datasets, which yielded higher SI starting as early as the fifth image acquisition.

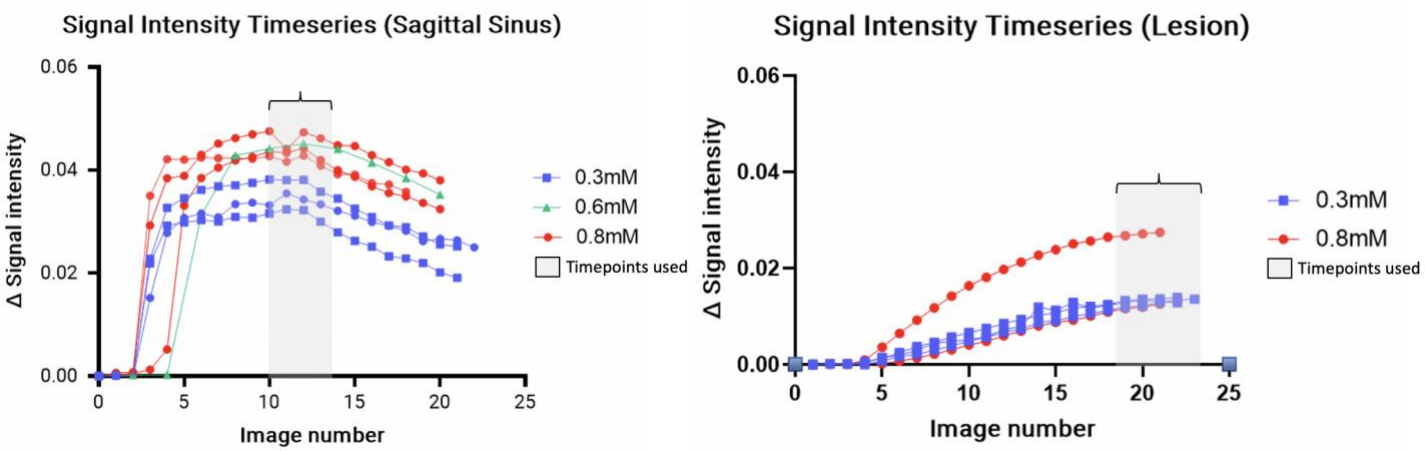

Figure 12. Signal intensity changes in the sagittal sinus (left) and the lesion site (right) per concentration of Gd

Below, in figure 13, we can inspect the Gd concentration maps for the three different concentrations that were injected. Specifically, we can see T1-weighted scans and the corresponding concentrations maps before CA administration, as well as the concentration maps when peak concentration was reached in the sagittal sinus, corresponding to the timepoints marked in grey in figure 12. Visually speaking, we can hence identify accumulations of CA both in the sagittal sinus and the lesion, as well as regions outside the brain parenchyma with ample blood supply.

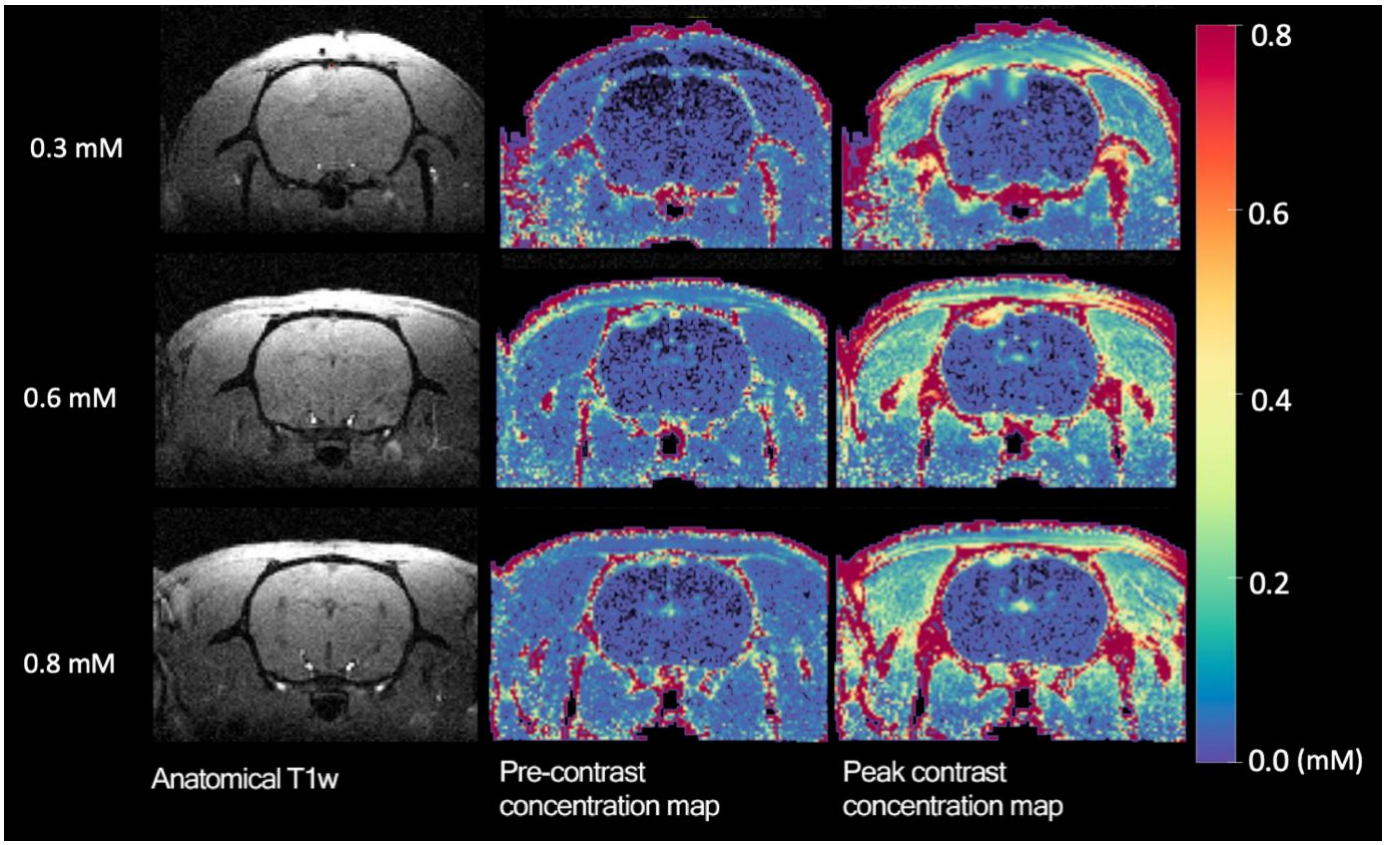

Figure 13. Anatomical T1-weighted scans and their respective pre- and peak concentration maps.

While these concentration maps gave us a visual representation of the distribution and concentration of the CA upon being infused, further quantifications needed to take place in order to assess their reliability and accuracy. The boxplots in figure 14, thus showcase the detected amounts of Gd both the sagittal sinus and the lesion, in each rat. Mean peak CA concentrations measured in the sagittal sinus were equal to 0.723mM (±0.09911, n=3) for the 0.8mM group, 0.6035mM (n=1) for the 0.6mM group and 0.4217mM (±0.07511, n=3) for the 0.3mM group. On the other hand, the mean peak CA concentrations measured in the lesion site were equal to 0.1425mM (±0.1441, n=2) for the 0.8mM group and 0.09158mM (±0.001954, n=2) for the 0.3mM group. A scatterplot visualizing the concentration ratios detected in lesion and sagittal sinus can be seen in appendix D.

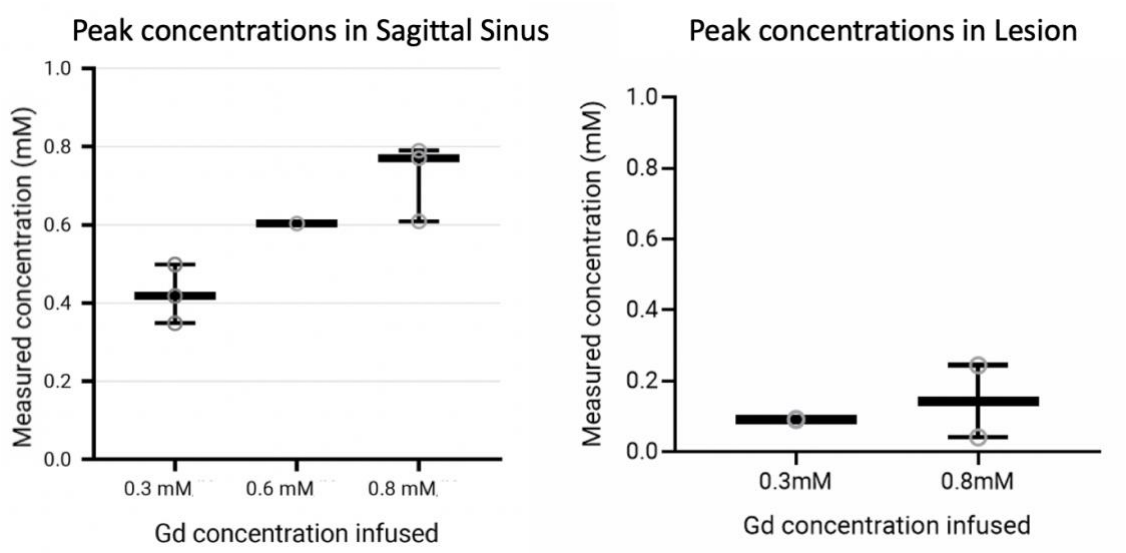

Figure 14. Boxplots depicting the mean Gd concentrations measured at timepoints of peak concentration levels.

4. Discussion

4a. Observations

First of all, we were successful in optimizing a step-down infusion protocol that allows sensitive measurements of Gd concentrations. By reducing the amount of liquid infused in the protocol by Nagaraja et al. (2007) by half, we were able to avoid any adverse physiological reaction in the rats, regardless of the concentration of Gd administered. This is an important step, as an innocuous manner of contrast agent administration will be a key pillar of the longitudinal study. Furthermore, adaptations of the stereotaxic coordinates for the PT stroke model were also well-implemented, as the lesions we induced were comparable to those in literature (Stoll et al., 2009; Kharmalov et al., 2003; Lapilover et al., 2012).

Especially, interesting was the development of secondary thalamic injury, as it confirms that the cortical areas affected by the induced stroke are functionally connected to various thalamic nuclei, providing further evidence that our lesions affect the intended cortical regions. Considering that ipsilateral thalamic diaschisis is also reported in human patients (Reidler et al., 2018), this observation hence further increases the clinical relevance of our study. We were able to detect this secondary thalamic degeneration as soon as 4 weeks post stroke onset. To explain the phenomenon, we have to consider that stroke can be seen as a disorder of brain connectivity (Cao et al., 2020), as a particular area of the brain affected by stroke can give rise to network-wide degeneration. The thalamus sustaining such degeneration following cortical stroke is thought to be a result of the thalamus' role as a relay station. The sudden lack of neuronal network activity input from the ipsilateral cortex leads to cell death. Specific to the setting of the PT stroke model, Dihné et al. (2002) also confirm that retrograde degeneration, i.e. neuronal destruction after axonal injury spreading backwards along the axon, toward and into the nerve cell body is the core cause for secondary thalamic injury in the PT model, which we observed. The relevance of secondary thalamic injury in PSE is still being examined, though according to Paz et al. (2013) it plays a key role in seizure maintenance, as thalamocortical neurons linked to the lesioned cortical areas sustain alterations in hyperpolarization-activated cyclic nucleotide–gated (HCN) channel expression, thereby turning hyperexcitable. As such, the thalamus provides itself as a region of interest for further investigation, i.e. to which extent the spatiotemporal characteristics of BBB disruption/leakage explain thalamic diaschisis, as questioned by (Cao et al., 2020) and in turn how it may be implicated in epileptogenesis.

Concerning the phantom scans, we initially aimed to validate the in-vivo findings, by comparing their SIs to those measured in the contrast-enhanced T1-weighted images. More specifically, we wanted to compare CA-linked SI enhancement in the lesion site and the sagittal sinus to the CA-linked SI enhancement in the phantoms (MnCl2 and blood respectively). In turn this would have allowed us to verify whether the in-vivo measures matched the phantom data. However, this was unsuccessful as in both phantom experiments SI increased non-uniformly, with tubes containing lower Gd concentrations showcasing higher SI than their counterparts actually containing a higher Gd concentration (see appendix E for visualization). As this was unlike any pattern described in literature, we performed a nonparametric nonuniformity normalization (N3) correction, in order to control for our surface coil. Unsurprisingly, the N3 correction overcorrected the top layer of phantom samples, smoothing SI across the image, which can be seen in figure 15.

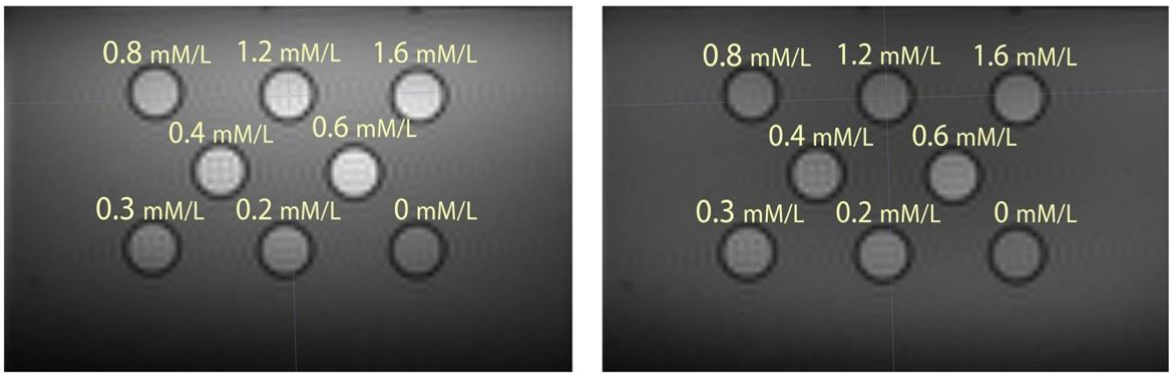

Figure 15. Coronal slice of T1w MnCl2 phantom pre- (left) and post N3 correction

Thus, it was also attempted to correct for B1 inhomogeneities/flip angle deviations via our B1-maps by computing a correction term. Likewise, this did not solve the problematic as even when correcting for flip angle deviations, the signal enhancement did not increase in a uniform manner. Presumably the reasons behind these issues were related the use of our surface coil, which could be circumvented by acquiring pre- and post-contrast scans to correct with. In order to acquire such pre- and post-contrast scans a more sophisticated phantom setup, such as the one used by Kim et al. (2017) is required, which allows the perfusion of CA into the phantom tubes during image acquisition. On the other hand, we were successful in retrieving relaxivity measures in MnCl2, which in turn allowed us to model the signal intensities as a function of increasing Gd concentrations for our T1-weighted sequence at the ultra-high field strength of 9.4T. In fact, this model allowed us to clearly demonstrated the impact of T2* on signal intensity.

In terms of the in-vivo contrast estimation, the calculations within the sagittal sinus proved to be within the range of Gd infused. In other words, based on the manually defined ROIs of the sagittal sinus the measured concentration levels increased with the actual CA concentration infused, with particular accuracy in the 0.6mM group. At the lesion site, less CA was detected, as less CA extravasated in this area. Temporally speaking, it took longer for CA to reach the lesion site, as peak CA concentrations were measured at the end of each acquisition. In comparison this was not the case for the sagittal sinus, where peak CA concentrations were reached halfway through imaging acquisition. In fact, successfully estimating concentrations in both tissue and blood is an essential step in modelling BBB leakage, and as such represents a crucial finding for the longitudinal study. However, to truly quantify leakage across the BBB, pharmacokinetic models are required, such as the Tofts or

Patlak model. A potential limitation of the Patlak model is that it assumes irreversible uptake without taking into account the reflux rate of Gd, which may provide accuracy issues in investigating BBB leakage. On the other hand, the Tofts model produces reliable values mainly when tissue is weakly vascularized or highly perfused (Sourbron & Buckley, 2011). Hence, our data must be used to assess which model attains the most accurate and reliable results for the purpose of investigating BBB leakage over multiple weeks.

4b. Limitations & future directions

Concerning the phantoms scans, multiple factors could be improved upon. Aside from the pre- and post-contrast measurements (surface coil corrections), a variable cited in literature that could affect our results is temperature. For instance, it has been recorded that the T1 in post-mortem scans or tissue samples fluctuates depending on temperature (Adolphi et al., 2013; Nelson & Tung, 1987). Thus, temperature may be a variable that should be controlled for, in order to improve the validity of the phantom scans. Especially when considering that the temperature in the scanner room is colder than average room temperature (± 20°C), and the agar had to be cooled down in order to solidify, our samples were likely below body temperature (± 37.5°C). As such, if phantom data is used to validate in-vivo findings, the temperature should be adjusted, or at least measured in order to correct for deviations.

Regarding the secondary thalamic injuries, we only assessed the thalamic sub-regions visually. Calculating the volume of this secondary degeneration could be valuable, as well as more accurate measurements of the site of injury. In fact, histology would be a valuable addition to present study. Not only to accurately assess the location of the secondary thalamic injury, but also to precisely delineate the cortical infarct induced via PT and more accurately describe the morphology.

Further, neither the actual epileptogenic aspect of PSE, nor behavioral factors were addressed in this study. As such video-electroencephalograms and behavioral/cognitive measures will be a valuable addition to this study, to assess functional recovery, as well as the development of epilepsy. While these measures will be included in the longitudinal study, they heavily impact the extent to which we can infer the potential incidence rate or potential PSE biomarkers within this study.

With reference to the methodology of generating the concentration maps, some improvements could be made via automation. Specifically, the amount of effort in manually delineating the sagittal sinus could be reduced while the accuracy of the resulting ROI mask could be improved by utilizing a script that automatically recognizes the sagittal sinus through the CA-influx related SI changes. Regarding the lesions, only scans within 1-week post PT stroke were used, however individual difference and edema may still affect the amount of extravasated CA. Further, we used an ROI mask that covered the entire lesion (see appendix F). Hence, we could also adjust the approach to drawing the ROIs, as perilesional tissue or certain pre-specified areas within the lesion (e.g. the core, superior and inferior areas) can also be compared.

5. Conclusion

Overall, the present pilot study was successful in examining the feasibility of the approaches intended to be used in the longitudinal study. While of course we cannot definitively state that we optimized the PT stroke for PSE, due to a lack of electroencephalograms, we replicated lesions seen in literature which reportedly led to PSE. Further, we also established a step-down infusion protocol that causes no harm to the experimental animal, and did in fact maintain the constant levels of CA during image

acquisition as shown by the SI timeseries. Additionally, due to the multiple scanning timepoints we were able to understand how the lesions evolve over the span of 8 weeks. Although secondary thalamic injury was recorded (starting as early as 4 weeks post-stroke), further biomarkers will need to be distinguished in the longitudinal study. However, given that the foundation for pharmacokinetic modeling has been established, more detailed analyses may now be conducted. That being said, we compared three different concentrations of Gd, to determine which will be the most beneficial in quantifying BBB leakage. As the 0.8mM concentration appears to yield the highest SI in the sagittal sinus, on face value it seems as if it would be the best approach to take. However, further investigations are needed to confirm its validity, as the sagittal sinus is heavily affected by T2*, which in turn affects SI and thus we may have to perform some corrections. Hence, the necessary methodology (i.e. MR sequences, CA infusion, lesion site, DCE-MRI data quantifications) for the longitudinal study are in place, whilst certain fine-tuning still needs to happen in the form of choosing the appropriate CA concentration and pharmacokinetic model.

References

Abbott, N. J., Patabendige, A. A., Dolman, D. E., Yusof, S. R., & Begley, D. J. (2010). Structure and function of the blood–brain barrier. *Neurobiology of disease*, *37*(1), 13-25.

Adolphi, N., Gerrard, C., Hatch, G., Takacs, N., & Nolte, K. (2013). Determining the temperature-dependence of tissue relaxation times (T1 and T2) for prospective optimization of post-mortem magnetic resonance (PMMR) image contrast. Journal of Forensic Radiology and Imaging, 1(2), 80.

Altman, K., Shavit-Stein, E., & Maggio, N. (2019). Post stroke seizures and epilepsy: from proteases to maladaptive plasticity. *Frontiers in cellular neuroscience*, *13*, 397.

Andersson JLR, Jenkinson M, Smith S (2010) Non-linear registration, aka spatial normalisation. FMRIB technical report TR07JA2

Armulik, A., Genové, G., Mäe, M., Nisancioglu, M. H., Wallgard, E., Niaudet, C., & Betsholtz, C. (2010). Pericytes regulate the blood–brain barrier. *Nature*, *468*(7323), 557-561.

Babb, T. L., Kupfer, W. R., Pretorius, J. K., Crandall, P. H., & Levesque, M. F. (1991). Synaptic reorganization by mossy fibers in human epileptic fascia dentata. *Neuroscience*, *42*(2), 351-363.

Bar-Klein, G., Klee, R., Brandt, C., Bankstahl, M., Bascuñana, P., Töllner, K., & Löscher, W. (2016). Isoflurane prevents acquired epilepsy in rat models of temporal lobe epilepsy. *Annals of neurology*, *80*(6), 896-908.

Berndt, P., Winkler, L., Cording, J., Breitkreuz-Korff, O., Rex, A., Dithmer, S., & Haseloff, R. F. (2019). Tight junction proteins at the blood–brain barrier: far more than claudin-5. *Cellular and molecular life sciences*, *76*(10), 1987-2002.

Busse, R. F. (2005). Flip angle calculation for consistent contrast in spoiled gradient echo imaging. *Magnetic Resonance in Medicine: An Official Journal of the International Society for Magnetic Resonance in Medicine*, *53*(4), 977-980.

Cao, Z., Harvey, S. S., Bliss, T. M., Cheng, M. Y., & Steinberg, G. K. (2020). Inflammatory responses in the secondary thalamic injury after cortical ischemic stroke. *Frontiers in neurology*, *11*, 236.

Conrad, J., Pawlowski, M., Dogan, M., Kovac, S., Ritter, M. A., & Evers, S. (2013). Seizures after cerebrovascular events: risk factors and clinical features. *Seizure*, *22*(4), 275-282.

David, Y., Cacheaux, L. P., Ivens, S., Lapilover, E., Heinemann, U., Kaufer, D., & Friedman, A. (2009). Astrocytic dysfunction in epileptogenesis: consequence of altered potassium and glutamate homeostasis?. *Journal of Neuroscience*, *29*(34), 10588-10599.

Deistung, A., Rauscher, A., Sedlacik, J., Stadler, J., Witoszynskyj, S. and Reichenbach, J.R. (2008), Susceptibility weighted imaging at ultra high magnetic field strengths: Theoretical considerations and experimental results. *Magn. Reson. Med.*, 60: 1155-1168. https://doi.org/10.1002/mrm.21754

Dihné, M., Grommes, C., Lutzenburg, M., Witte, O. W., & Block, F. (2002). Different mechanisms of secondary neuronal damage in thalamic nuclei after focal cerebral ischemia in rats. *Stroke*, *33*(12), 3006-3011.

Dobre, M. C., Uğurbil, K., & Marjanska, M. (2007). Determination of blood longitudinal relaxation time (T1) at high magnetic field strengths. *Magnetic resonance imaging*, *25*(5), 733-735.

Engel, O., Kolodziej, S., Dirnagl, U., & Prinz, V. (2011). Modeling stroke in mice-middle cerebral artery occlusion with the filament model. *Journal of visualized experiments: JoVE*, (47).

Feigin, V. L., Lawes, C. M., Bennett, D. A., Barker-Collo, S. L., & Parag, V. (2009). Worldwide stroke incidence and early case fatality reported in 56 population-based studies: a systematic review. *The Lancet Neurology*, *8*(4), 355-369.

Fieschi, C., Lenzi, G. L., Zanette, E., Orzi, F., & Passero, S. (1980). Effects of EEG of the osmotic opening of the blood-brain barrier in rats. *Life Sciences*, *27*(3), 239-243.

Galovic, M., Döhler, N., Erdélyi-Canavese, B., Felbecker, A., Siebel, P., Conrad, J., & Tettenborn, B. (2018). Prediction of late seizures after ischaemic stroke with a novel prognostic model (the SeLECT score): a multivariable prediction model development and validation study. *The Lancet Neurology*, *17*(2), 143-152.

Hagberg, G. E., & Scheffler, K. (2013). Effect of r1 and r2 relaxivity of gadolinium-based contrast agents on the T1-weighted MR signal at increasing magnetic field strengths. *Contrast media & molecular imaging*, *8*(6), 456-465.

Hallenbeck, J.M., & Dutka, A.J. (1990). Background review and current concepts of reperfusion injury. *Archives of neurology, 47 11*, 1245-54 .

Hoff, E. I., oude Egbrink, M. G., Viviane, V. T., Steinbusch, H. W., & van Oostenbrugge, R. J. (2005). In vivo visualization of vascular leakage in photochemically induced cortical infarction. *Journal of neuroscience methods*, *141*(1), 135-141.

Hughes, P. M., Anthony, D. C., Ruddin, M., Botham, M. S., Rankine, E. L., Sablone, M., & Perry, V. H. (2003). Focal lesions in the rat central nervous system induced by endothelin-1. *Journal of Neuropathology & Experimental Neurology*, *62*(12), 1276-1286.

Jenkinson, P.R. Bannister, J.M. Brady, and S.M. Smith. Improved optimisation for the robust and accurate linear registration and motion correction of brain images. NeuroImage, 17(2):825-841, 2002.

Karhunen, H., Bezvenyuk, Z., Nissinen, J., Sivenius, J., Jolkkonen, J., & Pitkänen, A. (2007). Epileptogenesis after cortical photothrombotic brain lesion in rats. *Neuroscience 148*(1), 314-324.

Karhunen, H., Nissinen, J., Sivenius, J., Jolkkonen, J., & Pitkänen, A. (2006). A long-term video-EEG and behavioral follow-up after endothelin-1 induced middle cerebral artery occlusion in rats. *Epilepsy research*, *72*(1), 25-38.

Kelly, K. M., Jukkola, P. I., Kharlamov, E. A., Downey, K. L., McBride, J. W., Strong, R., & Aronowski, J. (2006). Long-term video-EEG recordings following transient unilateral middle cerebral and common carotid artery occlusion in Long–Evans rats. *Experimental neurology*, *201*(2), 495-506.

Kelly, K. M., Jukkola, P. I., Yin, G., Miller, E. R., Kharlamov, E. A., Shiau, D. S., & Aronowski, J. (2018). Poststroke epilepsy following transient unilateral middle cerebral and common carotid artery occlusion in young adult and aged F344 rats. *Epilepsy research*, *141*, 38-47.

Kelly, K. M., Kharlamov, A., Hentosz, T. M., Kharlamova, E. A., Williamson, J. M., Bertram III, E. H., & Armstrong, D. M. (2001). Photothrombotic brain infarction results in seizure activity in aging Fischer 344 and Sprague Dawley rats. *Epilepsy research*, *47*(3), 189- 203.

Kelly, K. M., Kharlamov, A., Hentosz, T. M., Kharlamova, E. A., Williamson, J. M., Bertram III, E. H., ... & Armstrong, D. M. (2001). Photothrombotic brain infarction results in seizure activity in aging Fischer 344 and Sprague Dawley rats. *Epilepsy research*, *47*(3), 189-203.

Kharlamov, E. A., Jukkola, P. I., Schmitt, K. L., & Kelly, K. M. (2003). Electrobehavioral characteristics of epileptic rats following photothrombotic brain infarction. *Epilepsy research*, *56*(2-3), 185-203.

Kim, S. Y., Buckwalter, M., Soreq, H., Vezzani, A., & Kaufer, D. (2012). Blood–brain barrier dysfunction–induced inflammatory signaling in brain pathology and epileptogenesis. *Epilepsia*, *53*, 37-44.

Kim, H., Mousa, M., Schexnailder, P., Hergenrother, R., Bolding, M., Ntsikoussalabongui, B., Thomas, V., & Morgan, D. E. (2017). Portable perfusion phantom for quantitative DCE-MRI of the abdomen. Medical physics, 44(10), 5198–5209. https://doi.org/10.1002/mp.12466

Lapilover, E. G., Lippmann, K., Salar, S., Maslarova, A., Dreier, J. P., Heinemann, U., & Friedman, A. (2012). Peri-infarct blood–brain barrier dysfunction facilitates induction of spreading depolarization associated with epileptiform discharges. *Neurobiology of disease*, *48*(3), 495-506.

Lee, H., Mortensen, K., Sanggaard, S., Koch, P., Brunner, H., Quistorff, B., & Benveniste, H. (2018). Quantitative Gd-DOTA uptake from cerebrospinal fluid into rat brain using 3D VFA-SPGR at 9.4 T. Magnetic resonance in medicine, 79(3), 1568-1578.

Lee, K.R., Drury, I., Vitarbo, E., Hoff, J.T., 1997. Seizures induced by intracerebral injection of thrombin: a model of intracerebral hemorrhage. J. Neurosurgery. 87, 73e78.

Lippmann, K., Kamintsky, L., Kim, S. Y., Lublinsky, S., Prager, O., Nichtweiss, J. F., & Friedman, A. (2017). Epileptiform activity and spreading depolarization in the blood–brain barrier-disrupted peri-infarct hippocampus are associated with impaired GABAergic inhibition and synaptic plasticity. *Journal of Cerebral Blood Flow & Metabolism, 37*(5), 1803-1819.

Marchi, N., Granata, T., Ghosh, C., & Janigro, D. (2012). Blood–brain barrier dysfunction and epilepsy: pathophysiologic role and therapeutic approaches. *Epilepsia*, *53*(11), 1877-1886.

Mathern, G. W., Pretorius, J. K., Leite, J. P., Kornblum, H. I., Mendoza, D., Lozada, A., & Bertram III, E. H. (1998). Hippocampal AMPA and NMDA mRNA levels and subunit immunoreactivity in human temporal lobe epilepsy patients and a rodent model of chronic mesial limbic epilepsy. *Epilepsy research*, *32*(1-2), 154-171.

Nadareishvili, Z., Simpkins, A. N., Hitomi, E., Reyes, D., & Leigh, R. (2019). Post-stroke blood-brain barrier disruption and poor functional outcome in patients receiving thrombolytic therapy. *Cerebrovascular Diseases*, *47*(3-4), 135-142.

Nagaraja, T. N., Nagesh, V., Ewing, J. R., Whitton, P. A., Fenstermacher, J. D., & Knight, R. A. (2007). Step-down infusions of Gd–DTPA yield greater contrast-enhanced magnetic resonance images of BBB damage in acute stroke than bolus injections. *Magnetic resonance imaging*, *25*(3), 311-318.

Nelson, T. R., & Tung, S. M. (1987). Temperature dependence of proton relaxation times in vitro. Magnetic resonance imaging, 5(3), 189-199.

Öhman, J. (1990). Hypertension as a risk factor for epilepsy after aneurysmal subarachnoid hemorrhage and surgery. *Neurosurgery*, *27*(4), 578-581.

Paxinos, G. & Watson, C. *The rat brain in stereotaxic coordinates*. (Burlington MA Elsevier Inc., 2005).

Paz, J. T., Davidson, T. J., Frechette, E. S., Delord, B., Parada, I., Peng, K., Deisseroth, K., & Huguenard, J. R. (2013). Closed-loop optogenetic control of thalamus as a tool for interrupting seizures after cortical injury. Nature neuroscience, 16(1), 64–70. https://doi.org/10.1038/nn.3269

Reddy, D. S., Bhimani, A., Kuruba, R., Park, M. J., & Sohrabji, F. (2017). Prospects of modeling poststroke epileptogenesis. *Journal of neuroscience research*, *95*(4), 1000-1016.

Reidler, P., Thierfelder, K. M., Fabritius, M. P., Sommer, W. H., Meinel, F. G., Dorn, F., & Kunz, W. G. (2018). Thalamic diaschisis in acute ischemic stroke: occurrence, perfusion characteristics, and impact on outcome. Stroke, 49(4), 931-937.

Silverman, I. E., Restrepo, L., & Mathews, G. C. (2002). Poststroke seizures. *Archives of neurology*, *59*(2), 195-201.

Smith, S. M., Jenkinson, M., Woolrich, M. W., Beckmann, C. F., Behrens, T. E., Johansen-Berg, H., & Matthews, P. M. (2004). Advances in functional and structural MR image analysis and implementation as FSL. *Neuroimage*, *23*, S208-S219.

Smith, S.M., Fast robust automated brain extraction. *Human Brain Mapping*, 17(3):143-155, November 2002.

Sourbron, S. P., & Buckley, D. L. (2011). On the scope and interpretation of the Tofts models for DCE-MRI. *Magnetic resonance in medicine*, *66*(3), 735–745. https://doi.org/10.1002/mrm.22861

Stoll, G., Kleinschnitz, C., Meuth, S. G., Braeuninger, S., Ip, C. W., Wessig, C., & Bendszus, M. (2009). Transient widespread blood—brain barrier alterations after cerebral photothrombosis as revealed by gadofluorine M-enhanced magnetic resonance imaging. *Journal of Cerebral Blood Flow & Metabolism*, *29*(2), 331-341.

Sutula, T., Cascino, G., Cavazos, J., Parada, I., & Ramirez, L. (1989). Mossy fiber synaptic reorganization in the epileptic human temporal lobe. *Annals of Neurology: Official Journal of the American Neurological Association and the Child Neurology Society*, *26*(3), 321-330.

Tanaka, T., & Ihara, M. (2017). Post-stroke epilepsy. *Neurochemistry international*, *107*, 219-228.

Tanaka, T., Yamagami, H., Ihara, M., Motoyama, R., Fukuma, K., Miyagi, T., & Nagatsuka, K. (2015). Seizure outcomes and predictors of recurrent post-stroke seizure: a retrospective observational cohort study. *PLoS One*, *10*(8), e0136200.

Van Vliet, E. A., Otte, W. M., Gorter, J. A., Dijkhuizen, R. M., & Wadman, W. J. (2014). Longitudinal assessment of blood–brain barrier leakage during epileptogenesis in rats. A quantitative MRI study. *Neurobiology of disease*, *63*, 74-84.

Wang, G., Jia, H., Chen, C., Lang, S., Liu, X., Xia, C., & Zhang, J. (2013). Analysis of risk factors for first seizure after stroke in Chinese patients. *BioMed research international*, *2013*.

Wang, J. Z., Vyas, M. V., Saposnik, G., & Burneo, J. G. (2017). Incidence and management of seizures after ischemic stroke: systematic review and meta-analysis. *Neurology*, *89*(12), 1220-1228.

Watson, B. D., Dietrich, W. D., Busto, R., Wachtel, M. S., & Ginsberg, M. D. (1985). Induction of reproducible brain infarction by photochemically initiated thrombosis. *Annals of Neurology: Official Journal of the American Neurological Association and the Child Neurology Society*, *17*(5), 497-504.

Weber, R. Z., Grönnert, L., Mulders, G., Maurer, M. A., Tackenberg, C., Schwab, M. E., & Rust, R. (2020). Characterization of the blood brain barrier disruption in the photothrombotic stroke model. *Frontiers in physiology*, *11*, 1493.

Yang, H., Song, Z., Yang, G. P., Zhang, B. K., Chen, M., Wu, T., & Guo, R. (2014). The ALDH2 rs671 polymorphism affects post-stroke epilepsy susceptibility and plasma 4-HNE levels. *PLoS One*, *9*(10), e109634.

Zhang, B., Chen, M., Yang, H., Wu, T., Song, C., & Guo, R. (2014). Evidence for involvement of the CD40/CD40L system in post-stroke epilepsy. *Neuroscience letters*, *567*, 6-10.

Zhang, Y., Brady, M., & Smith, S. (2001). Segmentation of brain MR images through a hidden Markov random field model and the expectation-maximization algorithm. *IEEE transactions on medical imaging*, *20*(1), 45–57. https://doi.org/10.1109/42.906424

Zhao, Y., Li, X., Zhang, K., Tong, T., & Cui, R. (2018). The progress of epilepsy after stroke. *Current neuropharmacology*, *16*(1), 71-78.

Appendices

Appendix A: Serial dilution protocols

Blood phantom serial dilutions

Preparing 1.6mm gd+saline in blood solution:

- Prepare 100 µL solution from stock 1M Gd:
  - Take 100 µL Gd and dilute in 900 µL of saline
- Thereafter, take 10µL of the Gd+saline solution and add to 590µL of blood
  - Thus, we have 600 µL of solution containing 1.6mM.

1. Pipette 600 µL of 1.6 mM Gd&saline+blood into 0 µL of blood. (1.6mM)
2. Pipette 300 µL of dilution 1 (from step 1) into 300 µL of blood to create dilution 2. Mix well before continuing. Avoid generating bubbles. (0.8mM)
3. Pipette 300 µL of dilution 2 (from step 2) into 300 µL of blood to create dilution 3. Mix well before continuing. Avoid generating bubbles. (0.4mM)
4. Pipette 300 µL of dilution 3 (from step 3) into 300 µL of blood to create dilution 4. Mix well before continuing. Avoid generating bubbles. Discard 300 µL from dilution 4 to obtain the correct volume for the final dilution. (0.2mM)

→ Total amount of blood needed for this = **1.5ml**

Preparing 1.2mm gd+saline in blood solution:

- Prepare 100 µL solution from stock 1M Gd:
  - Take 100 µL Gd and dilute in 900 µL of saline
- Thereafter, take 7 µL of the Gd+saline solution and add to 593 µL of blood
  - Thus, we have 600 µL of solution containing 1.2mM.

5. Pipette 600 µL of 1.2 mM Gd&saline+blood into 0 µL of blood. (1.2mM)
6. Pipette 300 µL of dilution 1 (from step 1) into 300 µL of blood to create dilution 2. Mix well before continuing. Avoid generating bubbles. (0.6mM)
7. Pipette 300 µL of dilution 2 (from step 2) into 300 µL of blood to create dilution 3. Mix well before continuing. Avoid generating bubbles. Discard 300µL from dilution 3 to obtain the correct volume for the final dilution. (0.3mM)

→ Total amount of blood needed for this = 1.2ml + Control (300µL) = **1.5**

Grand total blood needed = 3ml

Dilution	Gd&saline+blood (µL)	blood (µL)	[Gd] (mM)
1	600 (from 1.6 mM stock)	0	1.6
2	300 (from dilution 1)	300	0.8
3	300 (from dilution 2)	300	0.4
4	300 (from dilution 3)	300	0.2

5	600 (from 1.2 mM stock)	0	1.2
6	300 (from dilution 1)	300	0.6
7	300 (from dilution 2)	300	0.3
8	0 (control group)	300	0

Manganese chloride phantom serial dilutions

Preparing 1.6mm Gd & MnCl2 solution:

- Take 160 µL from stock 1M Gd.
- Thereafter, add to 840 µL of 10mg/ml MnCl2 & saline solution.
    - Thus, we have 1000 µL of solution containing 0.16M.

1. Pipette 100 µL of 1.6 M Gd&MnCl2 into 900 µL of MnCl2 & saline solution (0.016M)
2. Pipette 100 µL of dilution 1 (from step 1) into 900 µL of MnCl2 & saline solution to create dilution 2. Mix well before continuing. (**1.6mM**)
3. Pipette 500 µL of dilution 1 (from step 1) into 500 µL of MnCl2 & saline solution to create dilution 2. Mix well before continuing. (**0.8mM**)
4. Pipette 500 µL of dilution 2 (from step 2) into 500 µL of MnCl2 & saline solution to create dilution 3. Mix well before continuing. (**0.4mM**)
5. Pipette 500 µL of dilution 3 (from step 3) into 500 µL of MnCl2 & saline solution to create dilution 4. Mix well before continuing. Discard 300 µL from dilution 4 to obtain the correct volume for the final dilution. (**0.2mM**)

Preparing 1.2mm Gd & MnCl2 solution:

- Take 120 µL from stock 1M Gd.
- Thereafter, add to 880 µL of 10mg/ml MnCl2 & saline solution.
    - Thus, we have 1000 µL of solution containing 0.12M.

6. Pipette 100 µL of 1.2 M Gd&MnCl2 into 900 µL of MnCl2 & saline solution. (0.012M)
7. Pipette 100 µL of dilution 1 (from step 1) into 900 µL of MnCl2 & saline solution to create dilution 2. Mix well before continuing. (**1.2mM**)
8. Pipette 500 µL of dilution 1 (from step 1) into 500 µL of MnCl2 & saline solution to create dilution 2. Mix well before continuing. (**0.6mM**)
9. Pipette 500 µL of dilution 2 (from step 2) into 500 µL of MnCl2 & saline solution to create dilution 3. Mix well before continuing. (**0.3mM**)

Dilution	**Gd&saline+blood (µL)**	**MnCl2 (µL)**	**[Gd] (mM)**
1	100 (from 0.016M stock)	900	1.6
2	500 (from dilution 1)	500	0.8
3	500 (from dilution 2)	500	0.4

4	500 (from dilution 3)	500	0.2
5	100 (from 0.012M stock)	900	1.2
6	500 (from dilution 1)	500	0.6
7	500 (from dilution 2)	500	0.3
8	0 (control group)	500	0

Appendix B: MRI scanning protocol

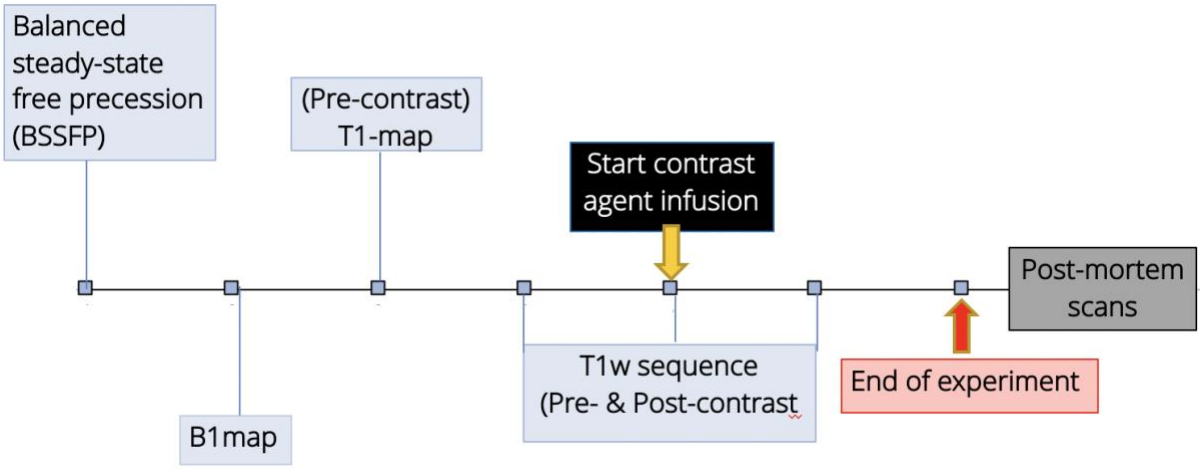

Appendix C: Registrations necessary for concentration maps

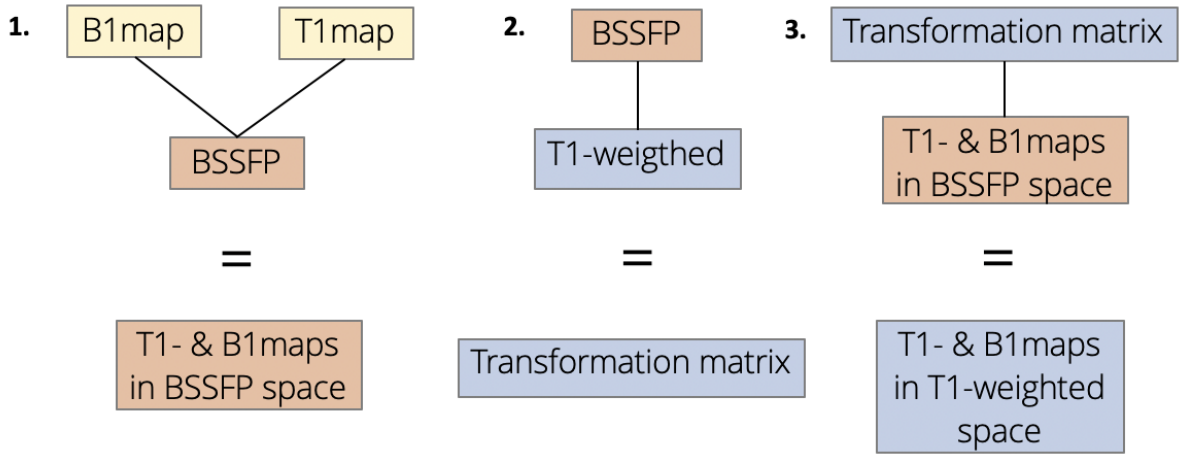

Appendix D: Concentration ratios measured per concentration

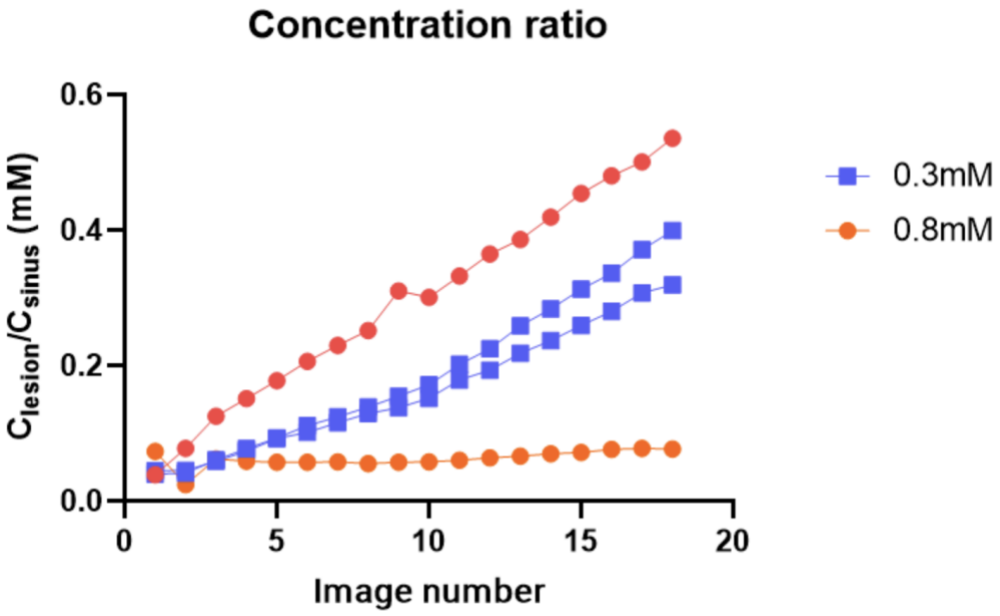

Appendix E: SIs measured in each tube of the MnCl2 phantom

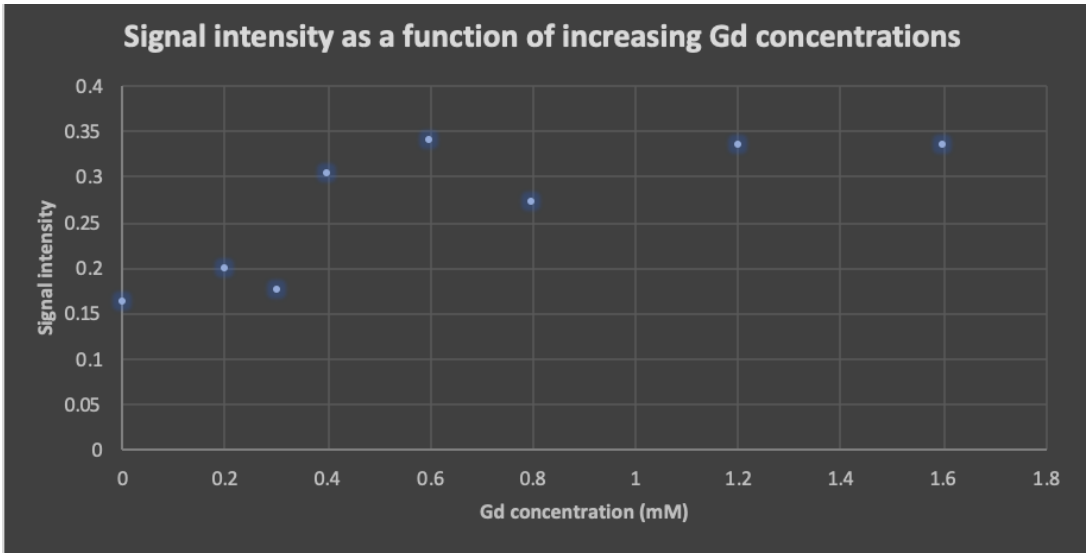

Appendix F: Lesion masks used for SI and CA concentration measurements